Optical Dipole Traps for Optimized Preparation of Ultracold Atomic Mixtures

用於優化製備超冷原子混合物的光學偶極阱

CHEN, Jun
陳軍

A Thesis Submitted in Partial Fulfilment
of the Requirements for the Degree of
Master of Philosophy
in
Physics

The Chinese University of Hong Kong

July 2014

Acknowledgement

First I would like to thank my supervisor, Prof. Dajun Wang, for giving me the opportunity to work in his group. It is Prof. Wang who shows me a big world where fascinating things are happening based on the interaction between the atoms and lights, and how the real scientists think and work. Prof. Wang's endless knowledge about ultracold physics is the constant support for the experiment, and he is also always there ready to help us not only with the projects we are taking but also with the matters about the life.

Also, I would like to thank my group members in the lab. The first time I come in the BEC lab at CUHK, it's senior graduate student Fudong Wang who showed me around and had a detailed introduction of the cool things they were doing. I learned a lot of experimental skills from former postdoc Dezhi Xiong, and I still remember the time when I saw the first saturation absorption spectroscopy signal with him. Senior graduate student Xiaoke Li has helped me deal with many theoretical problems. Graduate student Bing Zhu has a good intuition and can always give us good suggestions. Postdoc Xiaodong He has helped me a lot, without him my progress should be much slower or even impossible. Graduate student Mingyang Guo is hardworking and enthusiastic who also helped me a lot. I really cherish the time working with all you guys in the lab.

I acknowledge the help from many staff members in the physics department. Mr. W. K. CHAO has helped us deal with a lot of orders and Mr. Andrew S. K. LI borrowed us lots of general equipments. The staff members in the general office have also offered us many support. And the staff people in the machine shop helped us a lot with the fabrication of apparatus components.

Thanks also go to many of my friends here. In the difficult time we share the happy things and encourage each other. Your names are not here but the friendship from all of you will stay in my memory.

Last but not least, I would like to thank my parents and brother for their long time support for my study and every decision I have made.

Abstract

Ultracold mixture of atomic gases is a subject with many interesting applications. In this thesis, we present several recent developments in our lab on the production and exploration of a ^{23}Na and ^{87}Rb atomic mixture. These include optimized preparation of this mixture with a multi-wavelength optical dipole trap, a high field imaging system and the design of a "magic wavelength" optical trap.

The multi-wavelength optical trap is formed by superimposing a crossed 1070 nm trap with a single beam 660 nm trap. In this trap, the relative trap depth for Na and Rb can be tuned conveniently. By setting the trap depth for Na a little deeper than that for Rb we swap the role of coolant from Na to Rb in the evaporation process. This allows us to load more Rb atoms into the optical trap while lose less Na atoms during the evaporation. With the improved atomic mixture conditions, we have observed ^{23}Na^{87}Rb Feshbach molecules.

An important capability for polar molecule experiment is to detect molecules at high field. In this thesis an imaging system based on a DFB laser is designed, with which the cycling transition for imaging can be driven under high magnetic field. This laser system is also used for the residual atom removal in the molecule experiment.

For future experiments on dipolar physics, it is desirable to have a large sample of molecules. Currently, our Feshbach molecule number is limited by the low atom to molecule conversion efficiency. Part of the reason for this is the poor overlap between the two cloud centers due to the gravitational sags. To address this problem, a “magic wavelength” optical trap is designed and constructed with a homemade tapered amplifier. In this trap Na and Rb will see the same trap frequency. Thus the differential sag will be canceled and spatial overlap can be improved. With this improvement, the Feshbach molecule conversion efficiency should be enhanced and a larger molecule sample can be obtained.

論文摘要

超冷原子混合氣體是一個具有有趣應用前景的研究領域。在本文中我們將介紹幾個有關製備和探索^{23}Na和^{87}Rb超冷混合原子氣體的實驗進展， 包括基於一條多波長光學勢阱優化製備該混合氣體，高場成像系統，和一條“magic wavelength” 光阱的設計與搭建。

這條多波長光學勢阱由一條交叉雙臂的1070nm勢阱和一條單臂的660nm勢阱疊加而成。在該阱中，Na原子和Rb原子的相對勢深可以方便地控制。 當Na的勢深比Rb大時，Rb原子充當製冷劑而Na原子被協同冷卻。這使得我們在光阱蒸發時能裝載更多的Rb原子並且減少Na原子數的損失。 在該光阱的幫助下，我們成功觀察到了^{23}Na^{87}Rb Feshbach 分子。

在Feshbach分子實驗中，很重要的一步是在高場下探測分子數目。針對該難題， 本文中我們設計並搭建了高場成像系統。該系統基於一個我們自己搭建的DFB雷射器。 在該系統的幫助下高場成像得以實現。另外，由於工作頻率相同，在Feshbach分子實驗中該系統經證實 也能夠用於移除分子雲中的自由原子。

具有較多分子數的樣本對於將來進行與偶極相互作用有關的實驗是我們所追求的。 現階段分子數目主要受限於其轉化效率較低。一個重要的限制是由於重力的原因， Na和Rb原子雲並不重合。本文針對這個難題設計並搭建了一條“magic wavelength”光阱。在該光阱中Na和Rb具有相同的諧振頻率， 基於此，我們預期能觀察到同心的雙組份BEC。此外，在該光阱的幫助下，Feshbach分子數也會有較大提升。

Contents

List of Figures

List of Tables

Chapter 1

Introduction

1.1 General Context

The Bose-Einstein condensation (BEC) is a phenomenon that happens when an ensemble of identical particles are cooled below a critical temperature where the inter-particle distance becomes comparable with the thermal *de* Broglie wavelength of the particles, a macroscopical amount of particles can occupy in the same quantum state. This was first proposed by Bose and Einstein in 1924 [3, 4] from the quantum statistics theory, and realized in the lab with dilute atomic gases of ^{87}Rb and Na atoms in 1995 [5, 6], and subsequently in 1997 with Li atoms [7]. The achievement of the BEC is a landmark for the study in contemporary physics, which leads to the award of Nobel Prize in 2001 [8, 9].

The study of ultracold mixtures of two or more atomic species is one of the most interesting topics in ultracold physics. The ultracold mixture exhibits a lot of interesting phenomenons inaccessible in single species experiments. The controlled tunability of the interspecies or intraspecies interaction via the Feshbach resonance [10] further enriches the ultracold mixture system.

Among various experiments, the realization of the double species BECs and the formation of the Feshbach molecules has become one of the focuses. The double BEC is a good candidate for many research fields, such as the study of binary spinor physics [11, 12, 13], collision properties of the solitons [14, 15, 16], and miscibility-immiscibility phase transition [17, 18], et al. The ultracold polar molecule has a permanent electric momentum which enables us to study the long range, anisotropic dipole dipole interaction. In addition, when coupled with precise control the polar molecules will result in many interesting research fields, such as some new quantum phases: superfluid, supersolid, Mott insulator, checkerboard, and collapse phases et al [19, 20, 21, 22, 23]. The ultracold polar molecules will also be proved to be a good sample for the simulation of condensed matter physics, precision measurement, many body physics, quantum computation mediated by dipolar coupling between molecular qubits, and controlled ultracold chemistry [24, 25, 26, 27].

To date, several heteronuclear Feshbach molecules have been achieved in the two species mixtures, such as the ^{23}Na^{40}K [28], ^{23}Na^{6}Li [2], and ^{40}K^{87}Rb [29] in the Bose-Fermi mixtures, or the ^{41}K^{87}Rb[30] and ^{87}Rb^{133}Cs [31, 32] in the Bose-Bose mixtures, or the ^{6}Li^{40}K molecules in the Fermi-Fermi mixtures [33]. Among them, only the ^{40}K^{87}Rb molecules and the ^{87}Rb^{133}Cs molecules in the rovibrational ground state have been achieved [34, 35].

Our lab is working on the Na+^{87}Rb combination. The favorable background scattering length of the single specie of Na and ^{87}Rb makes itself stable with the background interaction and suitable for the study of binary BECs experiments with tunable interaction [36, 37, 1]. In addition, the ^{23}Na^{87}Rb molecule has a large dipole moment of 3.3D (1 a.u. ≈2.54 D) [38], and is immune to the exchange reaction $2\mathrm{Na}^{87}\mathrm{Rb} \longrightarrow \mathrm{Na}_2 + {}^{87}\mathrm{Rb}_2$ [39]. In the last a few years, our lab has achieved the dual species BEC and the Feshbach resonance between ultracold Na and Rb [1, 40]. After that we are already on the way pursing the ^{23}Na^{87}Rb molecules in the absolute ground state, and recently with some magic we have observed the ^{23}Na^{87}Rb Feshbach molecule signals.

1.2 This thesis

In this thesis, I will describe several improvements to the CUHK NaRb experiment implemented by me in the last two years. I will focus on the multi-wavelength optical dipole trap, which allows us to tune the relative trap depths between Na and Rb atoms. This improvement leads to a factor of 3 increases in the number of atoms for the double BEC and finally enables us to produce the NaRb Feshbach molecules. Several other works, including the high field absorption imaging and a "magic wavelength" optical trap with zero differential gravity sag will also be presented.

The organization of this thesis is as follows. In chapter 2, some theoretical background is introduced, including the properties of the alkali metal atoms, laser cooling and trapping principle, magnetic trapping, evaporation principle, and some BEC basics. In chapter 3, the experimental setup is described. Especially, we have given a detailed description of the properties of the external cavity diode laser (ECDL) and the laser frequency stabilization scheme for the Rb atoms. Chapter 4 to chapter 6 are the main part of this thesis. In chapter 4 we present the setup of the multi-wavelength optical dipole trap and experimental results. In chapter 5 the high field imaging system for the Feshbach molecule experiment is described. In chapter 6 the “magic wavelength” trap is described in which the double BEC of Na and Rb are expected to overlap well. In chapter 7 we close this thesis with a conclusion and some outlook for future work.

☐ End of Chapter.

Chapter 2

Theoretical Background

2.1 Atomic Properties of Alkalis

The development of ultracold atom experiment relies on the detailed understanding of the atomic structure, e.g. the fine structure, the hyperfine structure et al., and the interaction between the atom and light. The controlled external magnetic field supports us the manipulation of the spin degree of freedom. Thus, it is natural for us to take a look at the main properties of the atomic structure before focusing on the laser cooling and tapping process.

2.1.1 Atomic Structure

An alkali atom in the ground state has an unpaired electron in the outermost shell, e.g. 5s for Rb and 3s for Na. Due to the spin-orbit interaction ($\vec{L} \cdot \vec{S}$), the first excite state can be split into a doublet structure which is also known as the D_1 and D_2 line, with a total electron angular momentum J = 1/2 and J = 3/2 respectively. Where J is given by $\vec{J} = \vec{L} + \vec{S}$, and it must be in the range $|L - S| \leq J \leq L + S$. Here we will focus on the D_2

transition only.

Both the ground state and the first excited state can be further split due to the coupling between the electron's total angular momentum $\vec{J}$ and the nuclear spin angular momentum $\vec{I}$, which results in the hyperfine structure characterized by the total atomic angular momentum decided by $\vec{F} = \vec{J} + \vec{I}$. Also, F should take the values within the range of $|J - I| \leq F \leq J + I$. Both ^{87}Rb and ^{23}Na have nuclear spin $I = \frac{3}{2}$, thus their ground state, $J = \frac{1}{2}$, will be split into two hyperfine levels, i.e. $F = 1$ and $F = 2$. For ^{87}Rb, the splitting between these two levels is ∼6.8 GHz, while for Na, it's ∼1.77 GHz. For the first excite state of the D_2 line of ^{87}Rb ($5^2\mathrm{P}_{3/2}$) or Na ($3^2\mathrm{P}_{3/2}$), F can take the value of 0, 1, 2, or 3.

2.1.2 Zeeman Effects

Each of the above hyperfine levels has $2F + 1$ magnetic sublevels which represents the possible projections of the angular momentum wavefunction along the quantization axis, labeled as $m_F = F, F - 1, ..., -F$. The selection rules for these levels are $\Delta F, \Delta m_F = 0, \pm 1$, except for $\Delta m_F = 0$ when $\Delta F = 0$. For the laser cooling process, generally the special transition between $|F = 2, m_F = 2\rangle$ and $|F = 3, m_F = 3\rangle$, also known as the cycling transition, is used both for ^{87}Rb and Na due to the fact that the selection rules enable the atom repeatedly scattering photons at the transition frequency, which is the crucial principle of laser cooling and will be introduced in the next section.

Without external magnetic fields, the magnetic sublevels are degenerate. Within a magnetic field this degeneracy will be broken and these sublevels will be shifted differently with the appearance of a B-field dependent structure. In the weak magnetic field range, when the energy shift is small com-

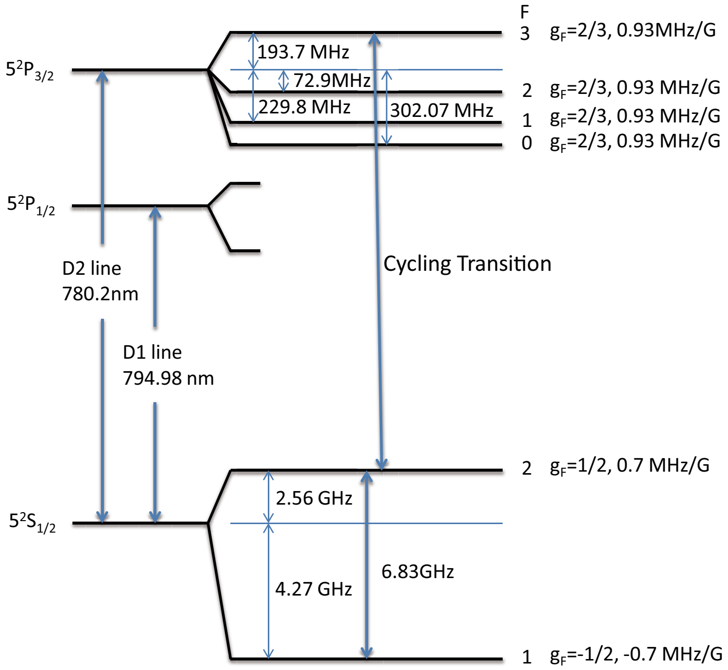

Figure 2.1: Levels diagram of the D_2 line of ^{87}Rb. The cycling transition is used for laser cooling and trapping. For the magnetic effect only a linear relationship is given in the low field region. The magnetic sublevels are not shown.

pared to the hyperfine splitting, F is a good quantum number and the energy shift can be expressed as [41]

$$\Delta E = \mu_B g_F m_F B_z, \tag{2.1}$$

where g_F is the landé g-factor. For the ground state of both ^{87}Rb and Na, $g_F=\frac{1}{2}$ and thus the Zeeman shift is ∼0.7 MHz/G. For their D_2 line, $g_F=\frac{2}{3}$ and the relationship is then 0.93 MHz/G which is shown in figure 2.1 and figure 2.2. If the magnetic field is so strong that the interaction energy dominates the hyperfine splitting, the coupling between the total atomic angular momentum $\vec{J}$ and the nuclear momentum $\vec{I}$ is then broken. This

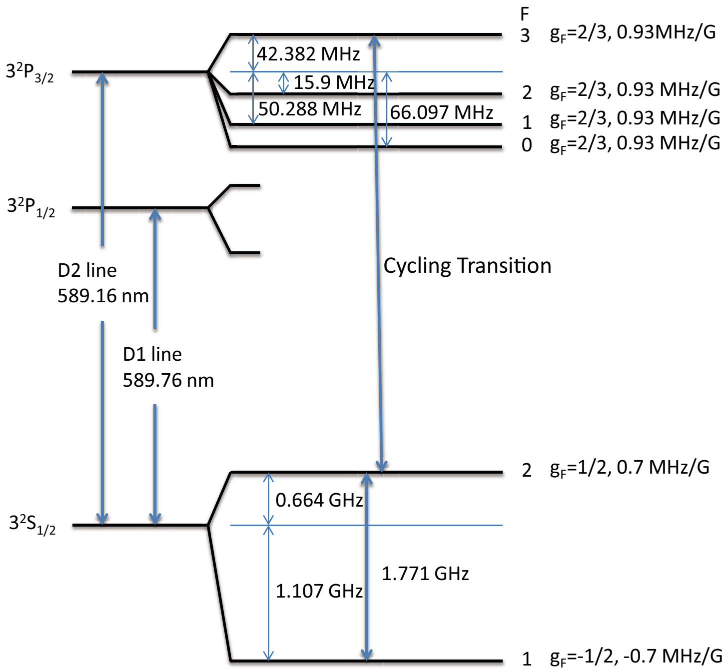

Figure 2.2: Levels diagram of the D_2 line of Na. Compared with ^{87}Rb, both the cycling transition and the magnetic effect in the low field region are the same, the only difference is the frequency spacing between the the levels.

is referred to as the Paschen-Bach effect, the energy shift can be calculated directly with formula from [42].

In our experiment, oftentimes the intermediate field is involved. In this regime, the energy shift is much harder to calculate and generally one needs to diagonalize the Hamiltonian which consists of the hyperfine splitting and the B-field induced energy shift. However, for the ground state the Breit-Rabi formula works very well. In picture 2.3 and figure 2.4 the energy of the hyperfine sublevels of the ground state in the B-field of both ^{87}Rb and Na is shown, from low field to strong field.

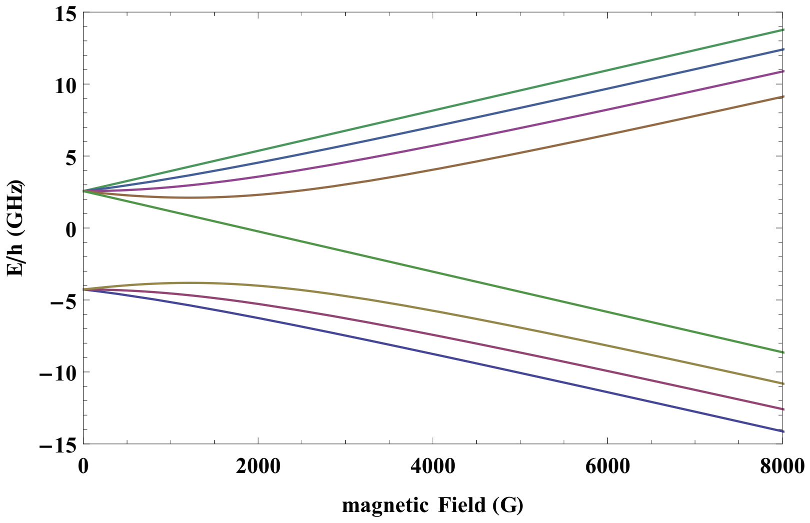

Figure 2.3: ^{87}Rb $5^2S_{1/2}$ (ground) level hyperfine structure in an external magnetic field.

2.2 Laser Cooling

Laser cooling is a technique which provides a powerful tool toward the ultracold temperature regime. Its discovery led to the award of the 1997 Nobel Prize [43, 44, 45]. To date, it is still a indispensable technique for ultracold quantum gas study. In this section, we will introduce the main principle of laser cooling as well as its limits. For more detailed description, one may refer to [46, 47] and reference therein.

2.2.1 Scattering Force

Fundamentally, the laser cooling process relies on the interaction between the atom and a near resonant light. The cooling laser linewidth is required to be smaller than that of the atomic transition, and the detuning is typically $< 3\Gamma$ (Γ is the atomic transition linewidth). For simplicity, we may take the atom as a two level system which has two kinds of cycles, i.e. the

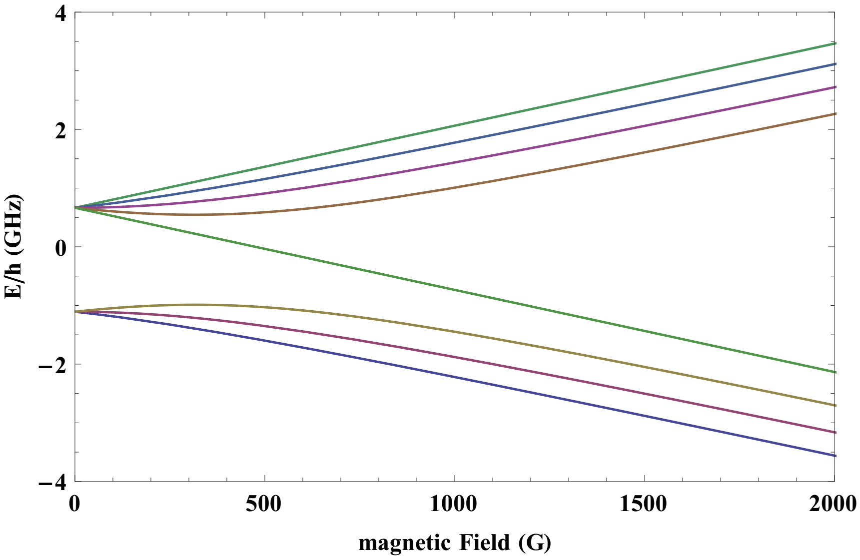

Figure 2.4: Na $3^2S_{1/2}$ (ground) level hyperfine structure in an external magnetic field.

stimulated emission or spontaneous emission with a stimulated absorption. Each absorption process imparts the atom a recoil velocity of $\vec{v}_{recoil} = \hbar\vec{k}/M$ (M is the mass of the atom). However, the spontaneous emission has a random direction, i.e. the time averaged momentum transfer of many circles of spontaneous emission is zero. For the stimulated emission process, the emitted photon just has the same momentum as the absorbed photon. Thus, after a single absorption-emission circle the net momentum transfer is just the photon recoil momentum, arising from which the scattering force can be obtained as:

$$\vec{F}_s = \hbar\vec{k} \cdot \frac{1}{2}\Gamma \frac{I/I_0}{1 + I/I_0 + (\frac{2\Delta}{\Gamma})^2}. \tag{2.2}$$

Where Δ is the laser detuning, I_0 is the saturation intensity, I is the light intensity.

2.2.2 Doppler Cooling

In the real situation, the atom has a velocity distribution which causes a Doppler shift typically on the order of 1 GHz at room temperature. The Doppler cooling technique addresses this issue by providing a velocity dependent force to the atoms. The schematic diagram of this process is illustrated in figure 2.5. The cooling mechanism can be understood as that for a stationary atom, the radiation force from the two counter-propagating lights with frequency ω slightly red detuned from resonance ω_0 can balance each other. For a moving atom the Doppler effect leads to the light opposite to the moving atom much closer to the transition, and the other beam further red detuned. As a result, the atom will be slowed down by the imbalanced

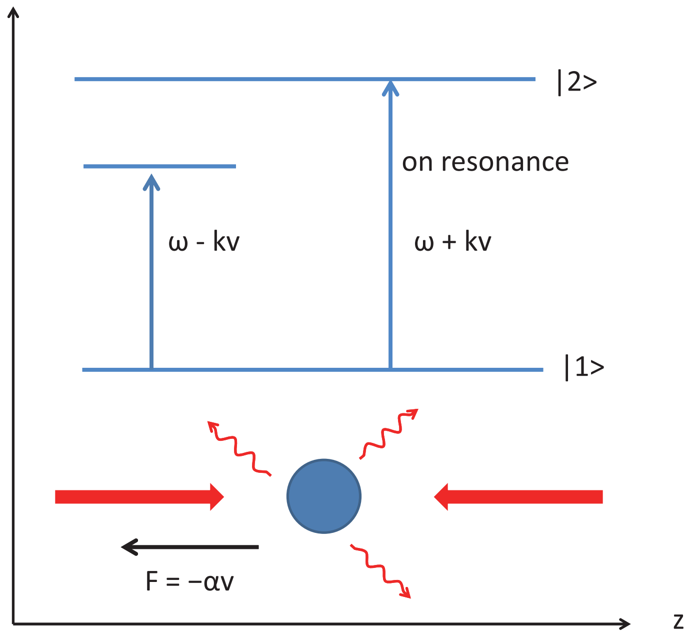

Figure 2.5: Doppler cooling principle shown in a 1-D case.

force from the two beams. The mathematical expression is

$$\begin{aligned} F_{molasses} &= F_{scatter}(\omega-\omega_0-kv) - F_{scatter}(\omega-\omega_0+kv) \\ &= \frac{\Gamma}{2}\hbar k \frac{I/I_0}{1+I/I_0+4(\frac{\Delta-kv}{\Gamma})^2} - \frac{\Gamma}{2}\hbar k \frac{I/I_0}{1+I/I_0+4(\frac{\Delta+kv}{\Gamma})^2} \\ &\simeq 8\hbar k^2 \frac{I}{I_0}\frac{\Delta/\Gamma}{[1+(2\Delta/\Gamma)^2]^2} v = -\alpha v. \end{aligned} \tag{2.3}$$

From which one may expect that the velocity can be reduced to 0. However, if we go back to the above discussion, we will find that though the random spontaneous emission ($\bar{v}=0$) has no net contribution to the momentum of the atom, it does has a kinetic energy ($\bar{v^2} \neq 0$) which leads to a heating effect. The balance between the cooling and heating determines the Doppler cooling limit:

$$T_{Doppler} = \frac{\hbar\Gamma}{2k_B} \tag{2.4}$$

As the atoms in a real gas are moving in all directions, generally three pairs of counter-propagating beams with nearly equal power are used to cool the atom cloud. For the D_2 line of ^{87}Rb and Na , $T_{Doppler}$ is 145 μK and 235 μK, respectively.

2.2.3 Sub-Doppler Cooling

The real atom has a much more complicated atomic structure (Zeeman sublevels) instead of the simple two levels system considered in the above. And the interference between the two counter-propagating laser beams may form a spatial varying light polarization. As a result, the atomic magnetic sublevels will experience a position dependent AC Stark shift. The additional light shift in turn acts on the atom as a potential well, along with spontaneous emitting, the atom can be further cooled by the process known as Sisyphus cooling [48, 49]. In this mechanism the cooling force has a much larger damping force which brings the atom to the sub-Doppler temperature regime. The limited temperature obtainable is the recoil limit:

$$\begin{aligned} T_{recoil} &= \frac{(\hbar k)^2}{M k_B} \\ &= \frac{2E_r}{k_B} \end{aligned} \tag{2.5}$$

2.3 Magneto-Optical Trap

The first MOT is realized and understood by a collaboration between MIT and Steven Chu's group [50]. To illustrate the main principle, we take a 1-D case as an example to show how the atoms get trapped, see figure 2.6. Consider the transition between S_0 (J=0) and P_1 (J=1) state. At the B field zero position (z=0) the Zeeman sublevels are degenerate. Away from the B-field zero, the magnetic sublevels will be split linearly with the atoms's position according to the Zeeman effect. And if the atoms are displaced from the trap center at $z < 0$ ($z > 0$), the $m_J = 1$ ($m_J = -1$) sublevel will be shifted down. If shine two slightly red detuned circular polarized beams with opposite handedness to these atoms, the Zeeman shift will drive this group of atoms much closer to the atomic transition. As a result the σ^+ (σ^-) transition will be excited and the imbalanced radiation force between the two beams will push the atoms toward the trap center.

Mathematically, it can be described as a combination of the laser cooling

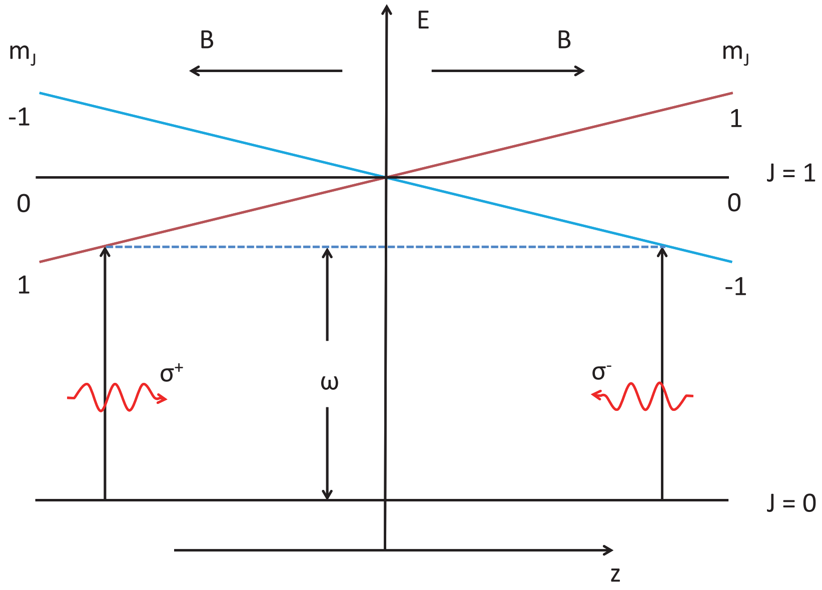

Figure 2.6: An 1-D example for illustrating the general principle of the MOT on a $J = 0 \leftrightarrow J = 1$ transition.

technique and Zeeman effect as [47]

$$\begin{aligned} F_{MOT} &= F^{\sigma^+}_{scatter}(\omega - kv - (\omega_0 + \beta z)) - F^{\sigma^-}_{scatter}(\omega + kv - (\omega_0 - \beta z)) \\ &\simeq -2\frac{\partial F}{\partial \omega}kv + 2\frac{\partial F}{\partial \omega_0 \beta z} \\ &= -\alpha v - \frac{\alpha\beta}{k}z, \end{aligned} \tag{2.6}$$

where $\beta z = \frac{g\mu_B}{\hbar}\frac{dB}{dz}z$ represents the Zeeman shift with displacement z. As we can see that F_{MOT} appears as a velocity and position dependent force.

In the real situation, the MOT is consisted of a small magnetic quadrupole field and three pairs of circular polarized counter-propagation beams with opposite handedness, see figure 2.7. The two coils are in the anti-Helmholtz configuration. In this case, at the position in the center of the coils $B = 0$. Close to this B field zero there is a linear magnetic field gradient in all

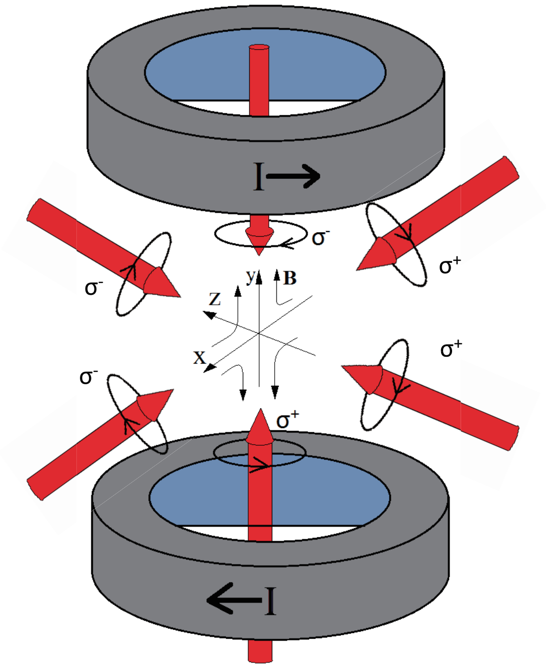

Figure 2.7: The schematic diagram of the MOT. A pair of anti-Helmholtz coils with counter-current produces the linear magnetic gradient field. Three pairs of beams with near equal power are circuit polarized with opposite handedness.

directions. From the Maxwell's equation $\nabla \cdot \overrightarrow{B} = 0$, we can see that

$$\frac{dB}{dx} = \frac{dB}{dz} = -\frac{1}{2}\frac{dB}{dy}.$$

2.4 Magnetic Trap

The magnetic trap takes advantage of the magnetic dipole moments of the neutral alkali atoms. The magnetic trapping comes out as a result of the Zeeman effect which we have discussed in the previous section. In a inhomogeneous field the atoms will experience a spatial varying potential which can be represented as:

$$V(r) = -\vec{\mu} \cdot \vec{B}(r), \tag{2.7}$$

where $\vec{\mu}$ is the magnetic dipole moment of the state. Taking the hyperfine splitting into consideration, it can also be written as:

$$V = g_F \mu_B m_F B. \tag{2.8}$$

One can immediately find that if for a certain state $g_F m_F > 0$ the atoms will be a low-field seeker and can be trapped around the B field minimum, while if $g_F m_F < 0$ it will be a high-field seeker and can not be trapped since the local maximum in a source-free region is impossible [51]. For the ground state of both ^{87}Rb and Na the trappable hyperfine states are $|2,2\rangle$, $|2,1\rangle$, as well as $|1,-1\rangle$ state at low field regime. Experimentally there are several configurations to realize the magnetic trap, such as the spherical quadrupole trap [52], time-averaged, orbiting potential (TOP) trap [5, 53], and Ioffe-Pritchard trap [54]. In our experiment the first one is employed due to its easy construction and efficient evaporation compared with the TOP trap or Ioffe-Pritchard trap with a parabolic potential shape [55].

2.4.1 Magnetic Quadrupole Trap

The Magnetic quadrupole trap is by far the easiest to construct, which is generated by a pair of anti-Helmholtz coils with opposite current directions. In this configuration the magnetic field vanishes at the trap center, and varies linearly with distances along all directions. Compared with the magneto-optical trap (MOT), it has the same B field but with much larger gradient. Thus we just apply the same coils but with different purpose in the experiment.

If we define the axial symmetry as the z direction, the trap center as the origin of the coordinates and choose the magnetic field gradient along x and y direction as $B^{'}$, according to $\nabla \cdot \vec{B} = 0$, the gradient along the z direction must be $-2B^{'}$. The amplitude of the field can be obtained as $B = B^{'}\sqrt{x^2 + y^2 + 4z^2}$, from which one can find it varies linearly from the trap center. The trap minimum at the center position also brings a main disadvantage for this trap. In the above discussion we have assumed that the atoms can remain in the same quantum state. This is true if the magnetic field seen by the atoms varies slowly with time, so that the atom quantum state can follow it adiabatically. But for a moving atom, it is then a time-dependent field instead of a static one, which may induce transitions between the states. As a result, a low field seeker may become a high field seeker which results in the atoms loss from the trap. If the field variation frequency is comparable or even larger than the transition frequency (on the Lamor frequency order) the trap loss will become severe. At the trap center (zero field position) there will be a "hole" where the atoms may flip their spin and then become lost. This is known as the Majorana loss. Though this trap by itself is unable to prevent the Majorana loss at low temperature, one can plug the Majorana hole by adding a blue detuned laser beam focused at the trap center, which is also known as the Optically plugged quadrupole trap [6], or focus a red detuned laser beam below or beside the quadrupole trap center to displace the overall potential minimum from the B field zero [56, 57, 1].

2.5 Evaporative Cooling

From the laser cooling section, one can see that although laser cooling is efficient, it can not bring us to the quantum regime. The PSD, ρ, of the sample is limited typically of the order of 10^{-5} [58, 59, 60, 61]. Thus, it is 5 orders of magnitude should be increased to reach the onset ($\rho \sim 1$) required by the BEC phase transition, i.e. further cooling is still in need, which should not only slow down the atoms but also increase the cloud density. This is achieved with the evaporative cooling technique [60, 62, 63, 64].

The basic idea for evaporative cooling is to selectively remove the atoms from the trap which carry away more than averaged thermal energy. After rethermalization the temperature of the remaining atoms will be reduced. In principle, the gradual removal of the atoms can continuously decrease the cloud temperature as long as there are enough atoms in the trap. Experimentally, the kinetic temperature of a few hundred of picokelvin (450 ± 80 pk) has been achieved by Ketterle's group via evaporating the Na BEC in the gravito-magnetic trap [65].

Evaporative cooling has lots of advantages over other techniques, e.g. laser cooling. Except for the great exceeded attainable temperature, its simplicity and wide temperature and density working range make it an irreplaceable step toward BEC. The major requirement is the thermalization time, which is set by the atom-atom elastic collision rate, should be short compared with the cloud lifetime. The evaporation efficiency, defined by the ratio of PSD gain to atom number loss as $\alpha = -\frac{log(\rho/\rho_0)}{log(N/N_0)}$, is usually used along with the initial condition to judge the atom number that can be condensed. The larger α means that the more energy than average can be removed. In principle, there is no up limit for α. However, the higher the efficiency the more time the process will take, which results in the heating and subsequent loss of the atoms due to inelastic collision process. On the other hand, with the decreasing of the cloud temperature, the evaporation speed will also decrease. Thus a trade-off between the evaporation efficiency and the evaporation speed is needed.

2.5.1 Microwave Evaporation

In the magnetic trap the most popular technique used to remove energetic atoms is the forced radio (RF) or microwave (MW) frequency evaporation. The basic idea is that the trapped atoms in the magnetic trap experiences a spatial varying Zeeman shift, according to $\frac{1}{2}m\overline{v^2} \approx g_F \mu_B m_F B$, the atoms with higher thermal energy then can be selectively driven from the trappable states to the non-trappable states with a resonant magnetic field. The most popular used scheme for ^{87}Rb is to transfer the atoms from $|1,-1\rangle$ to $|2,-2\rangle$ as illustrated in figure 2.8. In this way the ^{87}Rb atoms with energy greater than $U = \eta k_B T$ can be removed, where η is the truncation parameter which characterizes the threshold energy for evaporation. In the experiment situation, often η is kept as constant so that the lowing threshold energy is proportional to the decreasing temperature and one can lower the trap depth continuously without changing the trap frequency.

2.5.2 Evaporation in the Optical Trap

The spherical quadrupole trap can provide a tight confinement for efficient evaporation, however, it can not produce a BEC due to the severe Majorana loss at low temperature. Further evaporation toward BEC can be performed in the optical dipole trap. The trap depth is decreased by lowering the laser beam intensity so that one can selectly remove the energetic atoms from the trap. This method is first confirmed by Steven Chu's group who achieved a factor of 28 increase in the atomic PSD by trapping and evaporating the Na atoms in the optical trap formed by the intersection of two far detuned (1.06 μm) laser beams [66]. Compared with microwave evaporative

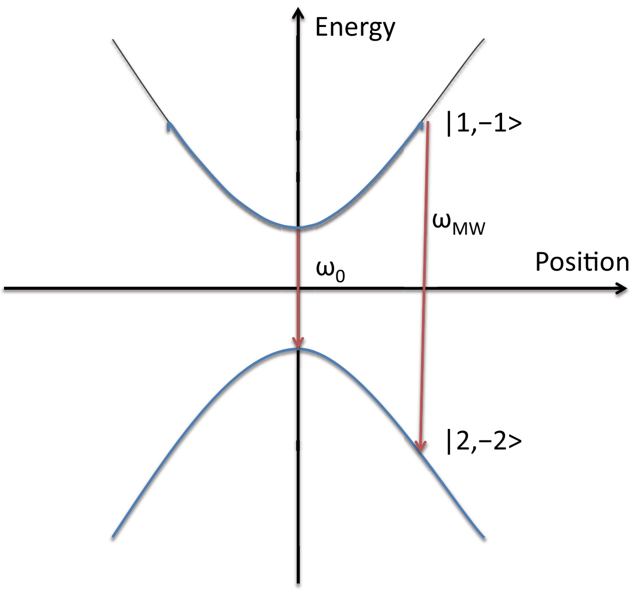

Figure 2.8: Microwave evaporation scheme for the ^{87}Rb atoms in a magnetic trap. An applied microwave drives the transition of the atoms with higher kinetic energy between hyperfine states of $|1, -1\rangle$ and $|2, -2\rangle$, by which way the energetic atoms can be removed selectly from the trap.

cooling, this method changes the trap volume thus has the advantage of designing the trap potentials (trap volume and depth), and optimization of the evaporation trajectory. The weakness of this method mainly comes from the decreasing confinement, hence the reduced cloud density and elastic collision rates, during the evaporation process. Though with these problems, several groups have achieved the BECs with different atoms by directly evaporating in the optical trap, e.g. [67, 68, 69, 70, 71].

2.6 BEC Basics

2.6.1 Bose-Einstein Distribution

For atoms with integer spin, i.e., bosons, at low temperature where quantum effects are important, the distribution of the atoms follow the Bose-Einstein distribution function [47],

$$f_{BE}(\varepsilon_i) = \frac{1}{e^{\beta(\varepsilon_i - \mu)} - 1}, \tag{2.9}$$

where $\beta = 1/k_b T$, and μ is the chemical potential which is responsible for the number conservation of the atoms. At high temperature the atoms are populated in all the levels with the occupation number for a specific state less than 1, which suggests that $\mu < \varepsilon_i$ according to Eq.(2.10). In particular, we could set $\mu < \varepsilon_0$ with ε_0 denoting the eigen energy of the ground state. With the decreasing of the atom temperature, the chemical potential will increase due to the requirement of the conservation of total atom number. However, the chemical potential can never exceed the ground state energy, i.e. ε_0, otherwise the distribution in the ground state will be negative. Thus, the maximum atom number in the excited state ε_i can be obtained is

$$N_i = \frac{1}{e^{\beta(\varepsilon_i - \varepsilon_0)} - 1}. \tag{2.10}$$

When the sum of the atom number in all the excited states has a number less than the total number N, the remaining atoms must stay in the ground state without upper limit for the atom number, which suggests the phase transition of the BEC.

2.6.2 BEC in a Harmonic Trap

Transition Temperature

The optical trap used to confine the ultracold atoms and perform the evaporation process toward BEC phase transition can be approximated as a harmonic potential [72]

$$V(\vec{r}) = \frac{1}{2}m(\omega_x^2 x^2 + \omega_y^2 y^2 + \omega_z^2 z^2), \tag{2.11}$$

where ω_i (i = x, y, z) is known as the trap frequency along the i direction. Generally, the transition temperature is given by [72, 73]

$$k_b T_c = \frac{N^{1/\alpha}}{[C_\alpha \Gamma(\alpha)\zeta(\alpha)])^{1/\alpha}}, \tag{2.12}$$

where $\Gamma(\alpha)$ is the *gamma function*, $\zeta(\alpha)$ is the *Riemann zeta function* and C_α is a constant. In the case of a 3 dimensional (3-D) harmonic trap, $\alpha = 3$, which gives $\Gamma(3) = 2$, $\zeta(3) = 1.202$, $C_3 = 1/(2\hbar^3\omega_x\omega_y\omega_z)$, and the critical transition temperature as

$$k_b T_c \approx 0.94\hbar\bar{\omega}N^{1/3}, \tag{2.13}$$

where $\bar{\omega} = (\omega_x\omega_y\omega_z)^{1/3}$ is the geometry averaged trap frequency used to characterize the trap volume. The onset of the BEC transition can also be represented by the PSD as $\rho = n\lambda_{dB}^3 > 2.612$, where λ_{dB} is the thermal *de* Broglie wavelength defined by $\lambda_{dB} = h/(2\pi m k_b T)^{1/2}$.

BEC Fraction

The atom number in the excited states (thermal atoms) can be given by

$$N_{th} = C_\alpha \Gamma(\alpha)\zeta(\alpha)(k_b T)^\alpha. \tag{2.14}$$

Which can be rewritten in terms of the transition temperature with Eq.(2.12) as

$$N_{th} = N(\frac{T}{T_c})^\alpha. \tag{2.15}$$

Thus, the fraction of the BEC as be obtained

$$N_0 = N[1 - (\frac{T}{T_c})^\alpha]. \tag{2.16}$$

Again, in the 3-D harmonic trap, $\alpha = 3$, the BEC fraction is

$$N_0 = N[1 - (\frac{T}{T_c})^3]. \tag{2.17}$$

Gross-Pitaevskii Equation

When the condensate is dominated by the two body interaction, which can be characterized by the s-wave scattering length a, and fulfil the condition $\bar{n}|a|^3 \ll 1$ the dynamical properties of the system can be well described by the Gross-Pitaevskii equation (GPE) [74, 75]

$$i\hbar \frac{\partial \Psi(r,t)}{\partial t} = (-\frac{\hbar^2}{2m}\nabla^2 + V(r) + g|\Psi(r,t)|^2)\Psi(r,t), \tag{2.18}$$

where $V(r)$ denotes the external potential, $g = 4\pi\hbar^2 a/m$ denotes the interaction with a referred as the s-wave scattering length. With the ansatz

$\Psi(r,t) = \Phi(r)e^{-i\mu t/\hbar}$ the time-independent GPE can be obtained which characterizes the static properties of the system

$$\mu\Phi(r) = (-\frac{\hbar^2}{2m}\nabla^2 + V(r) + g|\Phi(r)|^2)\Phi(r). \tag{2.19}$$

The density of the condensate is given by the mode square of the wavefunction as

$$n(r) = |\Phi(r)|^2, \tag{2.20}$$

with $N = \int |\Phi(r)|^2 dr$, which also reflects the shape of the wavefunction. Specifically, in a 3-D harmonic trap, the ground state function is given by

$$\Phi_0(r) = \frac{1}{\pi^{3/4}(a_1 a_2 a_3)^{1/2}} e^{-(\frac{x^2}{2a_1^2} + \frac{y^2}{2a_2^2} + \frac{z^2}{2a_3^2})}, \tag{2.21}$$

where $a_i = \sqrt{\hbar/(m\omega_i)}$ (i= x, y, z) is the width of the wavefunction in the i direction.

In most real systems the kinetic energy is small compared with the interaction term thus can be neglected, which turns out as the Thomas-Fermi approximation and from which the density can be obtained

$$n(r) = \frac{\mu - V(r)}{g} \tag{2.22}$$

In the harmonic trap the peak density locates at the trap center as

$$n_0 = \frac{\mu}{g}, \tag{2.23}$$

and reduce to zero at the Thomas-Fermi radius R, given by

$$R_i = \sqrt{\frac{2\mu}{m\omega_i^2}}. \tag{2.24}$$

The chemical potential can be solved with the normalization condition $N = \int |\Phi(r)|^2 dr$ as

$$\mu = \frac{\hbar\bar{\omega}}{2}(\frac{15Na}{a_{ho}})^{2/5}, \tag{2.25}$$

where $a_{ho} = \sqrt{\frac{\hbar}{m\bar{\omega}}}$ is the average harmonic length.

□ End of Chapter.

Chapter 3

Experimental Apparatus

3.1 Overview

The Na^{87}Rb mixture experiment is laid out on two independent optical tables. All the lasers and optics for generating light for laser cooling, repumping, optical pumping, and imaging are on one table. For ^{87}Rb, the laser system consists of two homemade diode lasers and a slave laser. While for Na, it's a ring dye-laser pumped by a diode-pumped solid-state (DPSS) laser (Lighthouse Photonics Sprout-G^{TM}, providing up to 6 Watts power at 532 nm in a near-perfect TEM$_{00}$ mode). It can output ¿ 600 mW power at 589 nm, which is enough for this experiment. All these lights are coupled into polarization maintained optical fibers and then delivered to the second table where our single-chamber vacuum system is housed. The detailed layout of the system will be described in this chapter. Since the setup of Rb and Na is pretty similar to each other (the main difference is the light frequencies and the laser) as an example, we set ^{87}Rb as an example.

3.2 Vacuum System

The cooling, trapping and all other manipulation of the atoms is within an ultrahigh vacuum chamber. Due to the collision between the cold atoms or molecules and the background gas which will result in the heating and subsequent loss of the atoms or molecules from the trap. The collision rate is $R_{loss} = n_b \bar{v_b} \sigma$, where n_b is the background gas density, $\bar{v_b}$ is the averaged velocity of the background gas and σ is the collision cross section. Early in 1992, the original BEC experiments argued that to make the re-thermalization time much shorter than the lifetime of the atoms in the trap, the vacuum should be in the range of 10^{-11} Torr [55]. Later on, with the appearance of the optical dipole trap, the lifetime of BEC is much longer [76]. However, in the case of the vacuum, less vacuum generally is better.

3.2.1 Vacuum Chamber

The vacuum chamber is a single rectangular glass cell without anti-reflection coatings. The outer dimensions of the cell is 100 mm× 40 mm× 40 mm. The pressure of the vacuum is maintained by an ion pump (Gamma Vacuum 45S). The initial vacuum is prepared following standard procedures. After that, the pressure reads from the ion pump controller is 1.3 $\times 10^{-11}$torr. The pressure at the center of the glass is estimated to be 5 to 6 times higher limited, which is verified by measuring the lifetime of the atoms in the magnetic trap.

3.2.2 Atomic Source

The atom source is a set of two Rb (Na) alkali atom dispensers (AMDs) from Alvatec GmbH, and is directly inserted into the glass cell from the backside of cube. These AMDs are electrically connected by spot-welding to the pins of an UHV feedthrough. Atoms can then be released when the AMDs are resistent heated. At the initial stage, to coat the glass cell with Rb (Na) atoms, we use a 2.5 A current to fire one dispenser for a whole day. After that, a 1.6 A current for the dispenser of Rb will provide enough Rb atoms source as well as a stable vacuum condition for the experiment.

3.2.3 Light Induced Atom Desorption

To achieve an efficient loading of the MOT, a large alkali vapor pressure is necessary. While for the slow evaporative cooling process, a long lifetime is desired. This put forward a contradiction in the experiment [77]. To overcome this, we use the light-induced atom desorption (LIAD) technique [77, 78, 79]. Generally, for the LIAD, different atom species may have different wavelength and power dependence. In our system, a 365 nm UV LED (Thorlabs M365L2) is employed, which has up to 200 mW output power. With this UV light, the enhanced loading rate of Rb MOT is observed, see figure 3.1. In addition, we point out that with another few UV lights covering different parts of the glass cell, the atom number loaded into the MOT may be further increased. Also, the recovery of the vacuum is observed in a short time after turning off the UV light, and the atom number loss is less than 10%.

3.3 MOT Laser System of ^{87}Rb

In this section, the optical layout of the home-made diode laser will be described first, followed by the spectrum properties. Then we will talk about the frequency stabilization scheme based on the saturation spectroscopy, and

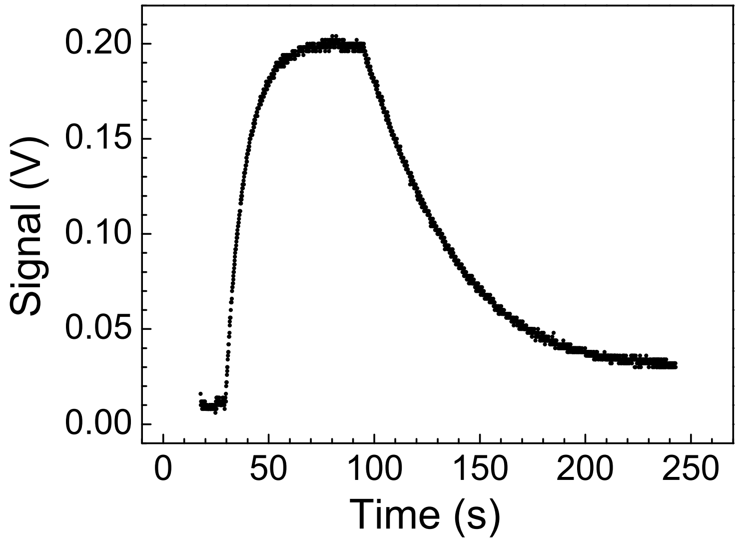

Figure 3.1: Strength of the fluorescence signal vs MOT loading time. The UV light is turned on at t ≈ 30 s, and turned off at t ≈ 90 s.

the injection locking scheme based on which the MOT light is created. In the final part the repump light and imaging light will be described.

3.3.1 Free Running Diode Lasers

In this section we will talk briefly about the diode laser. For more details, one may refer [80]. The center part of the diode laser is a semiconductor laser diode (Thorlabs DL7140-201S with output power 70 mW). With an injected current through the active region, the n-type and p-type cladding layers of the diode produce electrons and holes, which in turn recombine and emit photons. Laser action will occur until the current exceeds a threshold value, typically 35 mA, see figure 3.3. The diode behaves like a gain medium with a certain gain profile, whose width is about 25 nm centered at 785nm. Primarily, the lasing wavelength is determined by the band gap of the semiconductor materials, then determined by the junction's temperature and current density which could be used to tune the wavelength within the range determined by the gap. The back surface and uncoated output facet forms an intracavity etalon, whose length is very small. From $FSR = \frac{c}{2d}$, the free spectral range (FSR) of the free running laser will be very large, on the order of ∼100 GHz. And the width of each mode is above 25 GHz due to small cavity finesse, which is not narrow enough for laser cooling and trapping.

3.3.2 External Cavity Setup

To narrow the FSR of the diode, generally, the external cavity setup is used [81]. In brief, the rear facet of the diode and the grating forms the external cavity. From [82], the linewidth of a grating-stabilized diode laser decreases with square of the external cavity length, thus a reduction the linewidth by two orders of magnitude can be expected. In addition, the grating also enables the selectivity of the laser wavelength. The setup we use is in the Littrow configuration. The optical orientation is such that the first order reflected light from the grating is coupled back to the diode and the zeroth reflected light is used as the output light. The angle between the grating and the incoming light is decided by the grating equation: $\theta = arcsin(\frac{\lambda}{2 \cdot d})$, here d is the separation of the adjacent grooves on the grating. Figure 3.2 shows the schematic diagram of the diode laser.

In figure 3.4 the mode spectral of the grating stabilized diode laser is shown. The grating selectivity reflects the desired frequency from the broad range decided by the diode material. And this selected frequency is then fed back to the diode. This is referred as the gain profile of the grating. From the above grating equation, with $\sim$ 1cm external cavity length, the

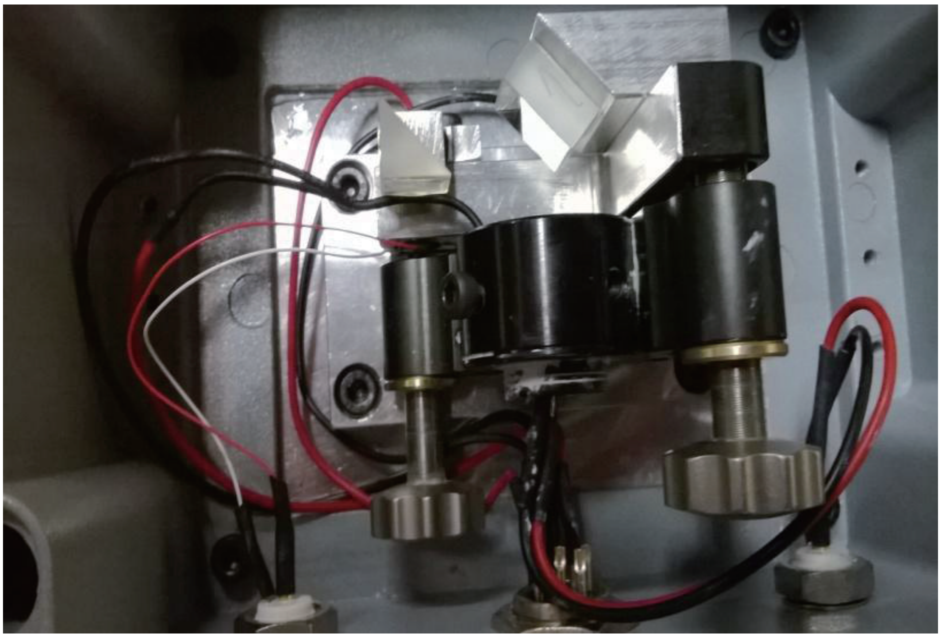

Figure 3.2: Schematic diagram of the grating stabilized diode laser in Littrow configuration. The external cavity enables both the reduction of the linewidth of the laser to less than 100 KHz and the laser frequency selectivity.

FSR then is on the order of ∼10 GHz which is ten times smaller than that of the internal cavity (∼100 GHz). The emitted frequency of the laser is then determined by the position where the gain profiles of the medium, internal cavity and external cavity can be overlapped well. Due to the stabilization of the grating, the linewidth of the emitted frequency can be less than 100 KHz.

The frequency of the laser can be adjusted by changing the angle of the grating in combination with the temperature and the current. In addition, to make the laser working with low noise, a low noise current driver (Thorlabs LDC202C) and a stable temperature controller (Thorlabs TED 200C) are required. The thermistor (RS Hong Kong B57550G203F) is directly inserted into the diode holder wall to measure the temperature. And the TEC (RS

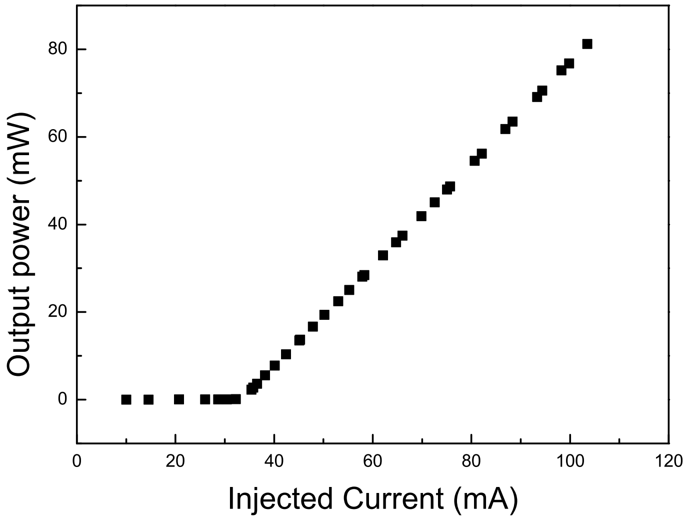

Figure 3.3: Threshold measurement of the grating stabilized Diode laser in Littrow Configuration.

Hong Kong CP1.0-127-05L) is placed between the bottom of the box and the diode holder.

3.3.3 Frequency Stabilization

For laser cooling and slowing of atoms, the laser's frequency needs to be actively controlled. This generally means locking the laser frequency to a reference standard. The natural choice is an atomic transition of Rb, with help of a Rb vapor cell. In our lab, the frequency modulation spectroscopy method [83, 84] has been chosen as the standard technique.

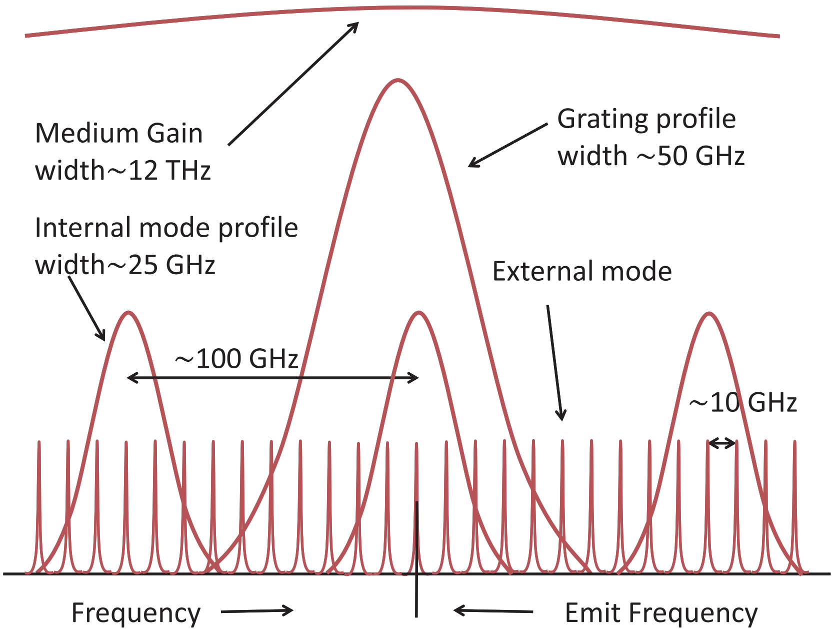

Figure 3.4: Gain profile of the medium, internal cavity, external cavity, grating, and based on which the emitted laser frequency is decided.

Saturation Absorption Spectroscopy

Experimentally to lock the laser to the frequency standard, i.e. the atomic transition position, we need to “see” the corresponding hyperfine structure of the atoms based on which the error signal can be obtained. This is obtained with the saturation absorption spectroscopy technique, which is a fundamental method to gain sub-Doppler resolution.

Taking the two level system as an example. The basic principle is that, at low intensity if we shine a laser beam to a random sample of atoms, the atom density will not be altered in each level. And the lower level number density has a Gaussian distribution of the velocity characteristic of the Doppler broadening of width $\Delta\omega/k$. The upper level will only have a negligible population. At high intensity, the stimulated absorption will be balanced by the stimulated emission with the group of atoms with velocity $v = (\omega - \omega_0)/k$. This means the population difference between two levels is reduced as soon as the atoms are excited to the excited state. This is referred to as the hole burning effect. The width of the hole is decided by $\nabla\omega_{hole} = \Gamma(1 + \frac{I}{I_{sat}})^{\frac{1}{2}}$, as shown in figure 3.5.

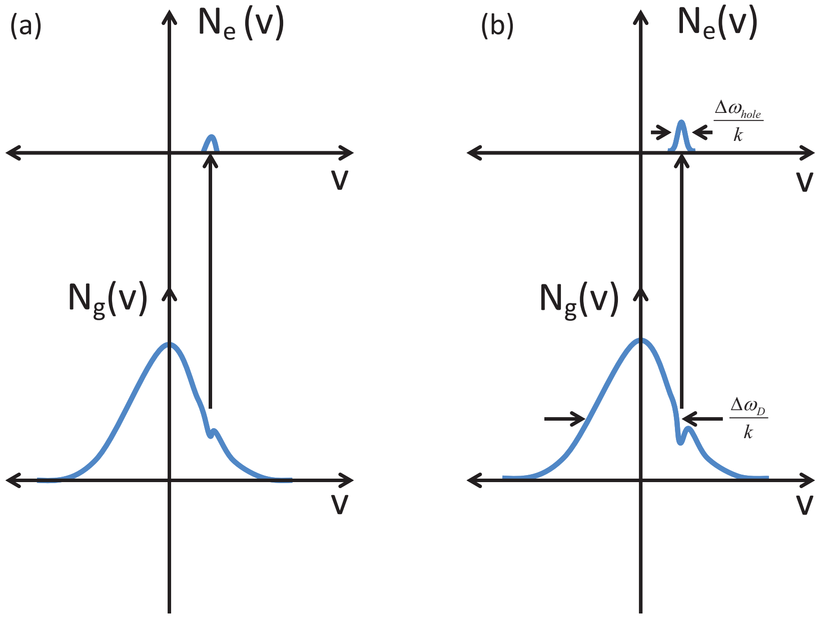

Figure 3.5: The saturation of absorption. (a) A week beam interacts with a random sample of atoms which has no significant affect on the population difference. (b) An intensive beam interacts with the same group of atoms, which alters the population difference obviously.

Real atoms generally have multiple upper and lower levels, which make the above process much more complicated. In our case for the Rubidium-D_2 transition, the ground state hyperfine splitting is more than 6.8 GHz which is far more than the Doppler broadening (with typical width 1 GHz at room temperature), while for the first excited state $5^2P_{3/2}$ the whole hyperfine splitting is about 495 MHz. This implies that the profile of the spectroscopy of ^{87}Rb F=2 $\longleftrightarrow$ F$^{'}$, or ^{87}Rb F=3 $\longleftrightarrow$ F$^{'}$, ^{85}Rb F=2 $\longleftrightarrow$ F$^{'}$, and ^{85}Rb F=3 $\longleftrightarrow$ F$^{'}$ will be the summing up Doppler profile of each hyperfine levels. Besides, there is another important resonance at frequency $(\omega_1+\omega_2)/2$, which is also called the cross-over resonance forms at position midway between two saturated absorption peaks. Due to this reason, it appears as the most pronounced feature in the spectrum and becomes the natural choice for laser stabilization.

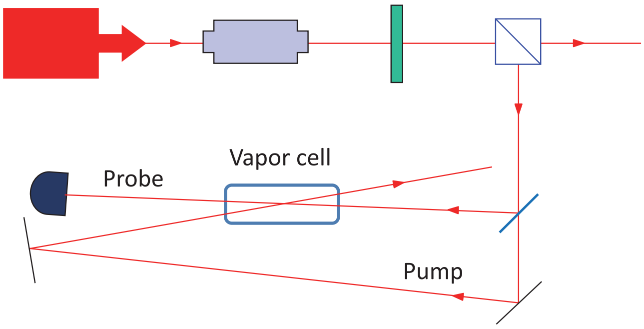

Figure 3.6: Experimental setup of the saturation absorption spectroscopy.

The experimental setup of the saturation absorption spectrum is shown in figure 3.6. The pumping and probing beams are produced with a glass plate which works as a beam splitter, i.e. splits the single laser beam into two beams with different strength by transmission (transmittance ~94%) and reflection (reflectance ~6%) respectively. The pumping beam is then reflected by two mirrors so that it will propagate through the Rb vapor cell in the opposite direction as the probing beam and more importantly to achieve good overlapping with the probing beam inside it. The probing beam is detected by a homemade photodiode which can transform the absorption spectrum into a voltage signal which can be seen directly with a oscilloscope.

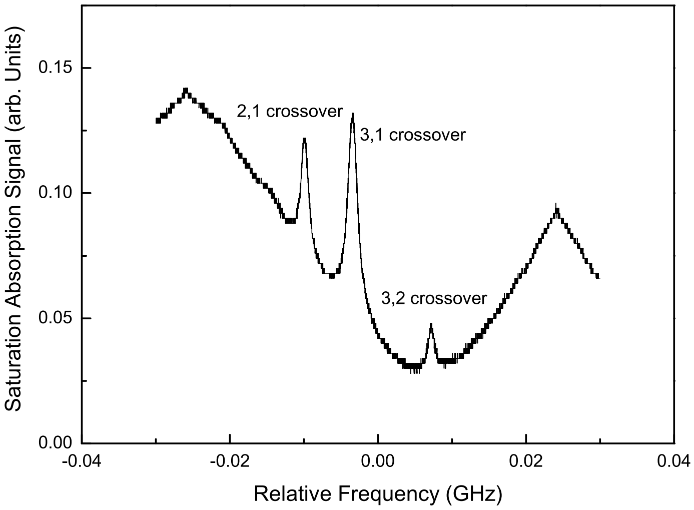

Figure 3.7: Saturation absorption spectroscopy of the F=2 ↔ F$'$ transitions of ^{87}Rb. The three absorption peaks from left to right corresponding to the (2,1), (3,1), and (3,2) crossover resonance respectively, which appears much larger than the hyperfine resonances obviously.

Laser Frequency Stabilization

To achieve precision locking, we choose to lock the laser at the absorption peak. But if we pay more attention to the saturation spectroscopy in figure 3.7, we will see that the signal is symmetrical around a resonant frequency, which means it cannot be used as a error signal as we can not identify whether a positive or negative feedback should be used with a frequency deviation. The modulation spectroscopy method can address this problem.

In figure 3.8 we show two typical error signals for laser trapping and repumping which corresponding to ^{87}Rb D$_2$ transitions F=2 ↔ F$'$ and F=1 ↔ F$'$, respectively. The steepest slopes corresponding to the cross-over resonances. With these error signals the laser then can be locked with a feedback

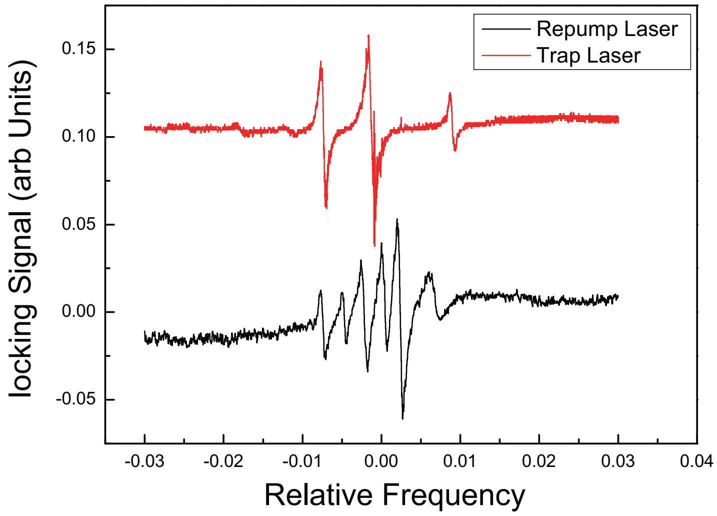

Figure 3.8: The error signal obtained from the current modulation method and can be used to lock the trap laser and repump laser respectively.

circuit.

3.3.4 Inject Locking

In the laser cooling process as can be seen from the above that actually three pairs of beams are used and each one is with about the same power, i.e. 18 mW out from the fiber. This puts forward another requirement for the laser–the power. However, the above described ECDL has a maximum output power 50 mW which is not sufficient enough to capture the atoms. The need of more power at the desired frequency leads to the development of the inject locking method. This is done by coupling a few percent (∼200 μW) of the locked laser power (master laser) into a free running laser (slave laser).

3.3.5 Optical Layout

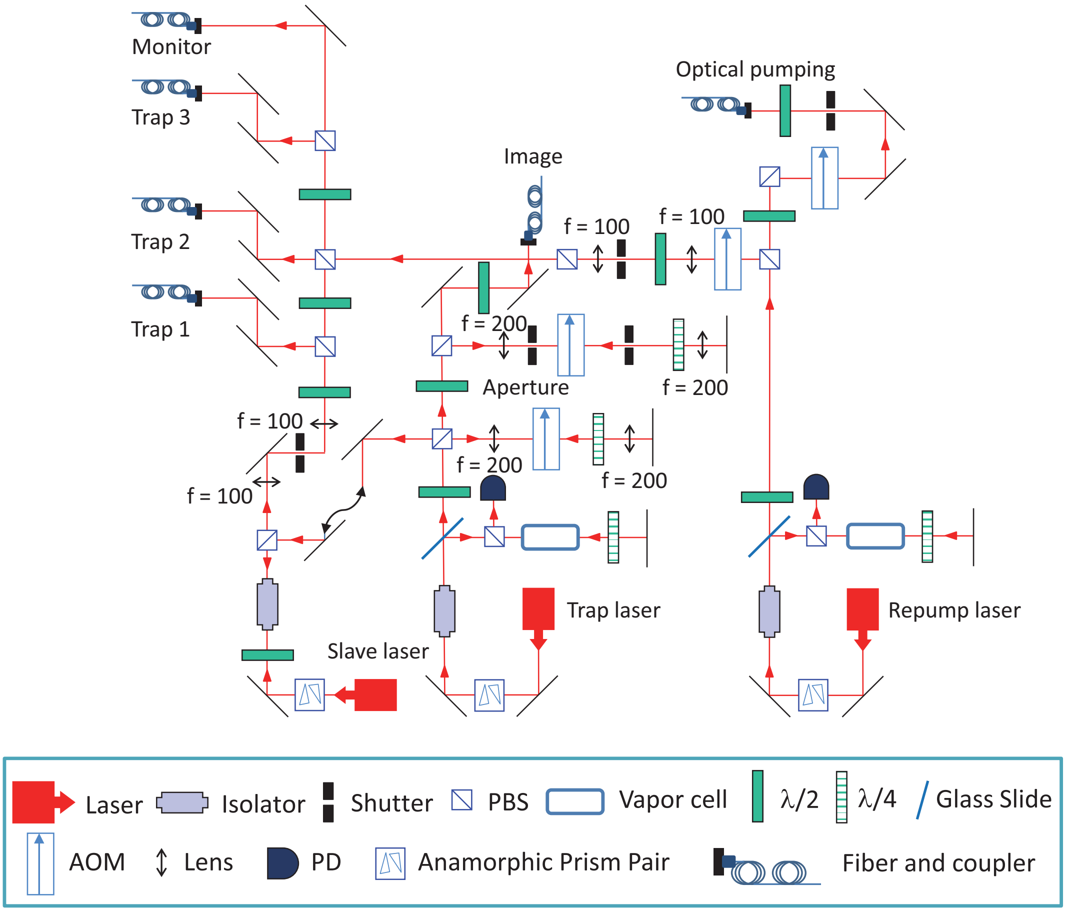

Figure 3.9: Optical layout of the MOT laser system for Rb

The optical layout of the MOT laser system is shown in figure 3.9 for Rb and in figure 3.10 for Na. The light beams with demanded frequencies can be obtained and tuned conveniently with the AOM for laser cooling and trapping as well as imaging, et al.

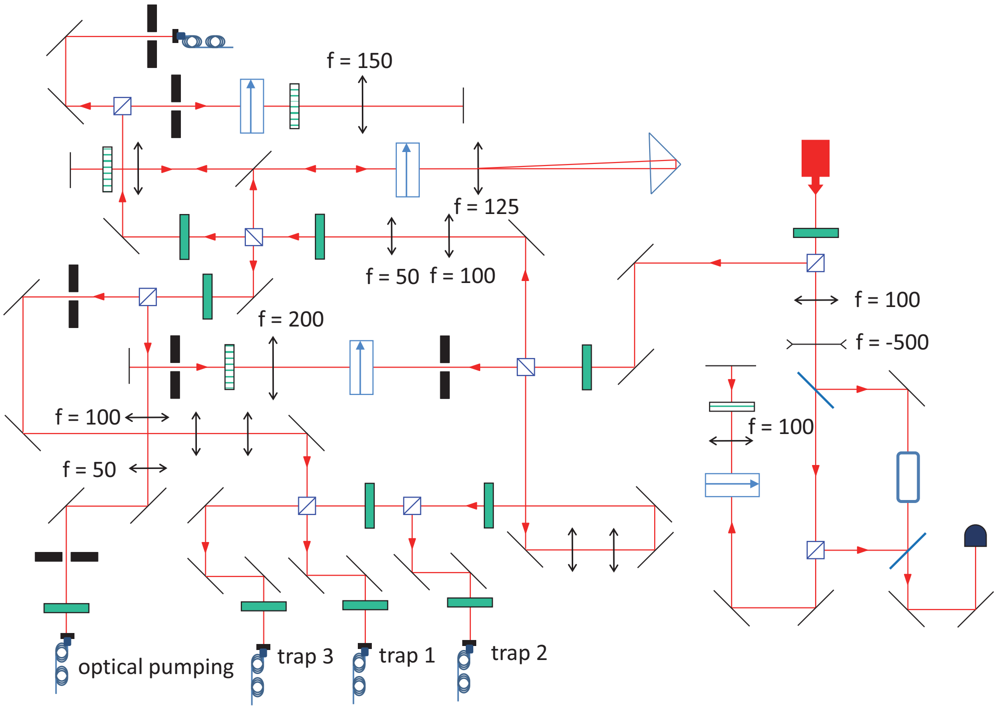

Figure 3.10: Optical layout of the MOT laser system for Na

Four-Pass AOM

A striking highlight in the optical layout of the MOT laser system of Na is the application of the four-pass AOM scheme, as shown in figure 3.11. The s-polarized incident beam is coupled to the AOM for the first pass, and a 2-inch lens (f = 125 mm) along with a right-angled prism enables a double pass scheme. The output beam is then picked off from the closely spaced incident beam via a horizontally mounted D-shaped mirror, after which another 2-inch lens (f = 125 mm) and a mirror enable the second double pass, i.e. by reversing the direction of the output beam of the first double pass. The output beam of the four pass scheme is immersed in the incident light, and a $\lambda/4$ wave plate and a PBS enable the separation of the two beams.

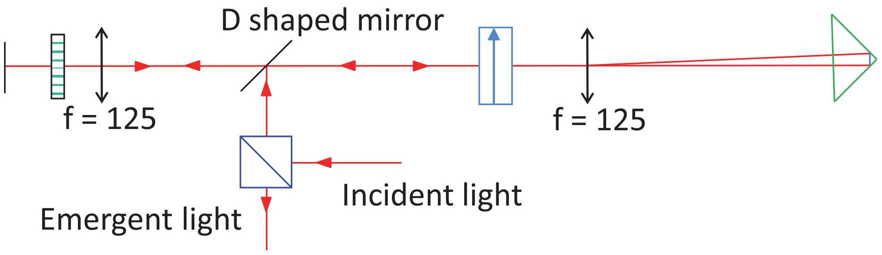

Figure 3.11: Schematic diagram of the four pass AOM (side view). A 2-inch lens (f = 125 mm) along with a right-angled prism enables a general two pass scheme. The two 2-pass schemes are coupled with a horizontally mounted D-shaped mirror. A PBS and a $\lambda/4$ wave plate is used to separate the emergent light from the incident light.

3.4 Loading the Magnetic Trap

Laser cooling is efficient to slow down the atoms to the 100 μK regime which already enables one get into the ultracold regime. However, it is still too hot for the BEC. To reach even lower temperature, we need to use the evaporative cooling technique in a magnetic or optical trap. Compared with the optical trap, the magnetic trap usually has a deeper trap depth and a larger trap volume. Thus, in our experiment toward dual species BECs of Rb and Na, the atoms are firstly loaded from the MOT to a magnetic trap for RF induced evaporative cooling followed by further evaporative cooling in the optical trap.

However, the atomic gas in the MOT usually occupies a relative large volume and also is not necessarily located at the lowest hyperfine state, which will lead to atoms number loss in the magnetic trap if nothing is done. This makes the intermediate stages necessary, i.e. the compressed MOT stage (C-MOT), optical molasses and optical pumping state, which aims at increasing the atom density as well as minimizing the potential energy picked up by the atoms, a process known as mode matching.

3.4.1 CMOT

The COMT process is performed by reducing the repump power to ∼150 μW and increasing the trap detuning from -19 MHz to -32 MHz for both species. This is to decrease the rate of the photons scattered by the atoms during the re-absorption process, hence the decreased heating rate to the cloud and an increased atom density. The optimized 24 ms COMT process also allows the realignment of the cloud center to that of the magnetic trap, which can minimize the potential energy gained by the atoms during the atom loading process from the MOT to the magnetic trap.

3.4.2 Optical Molasses

In the CMOT stage one can increase the atom density at the cost of the cloud temperature, which seems conflicts with our initial goal. However, as we can see from the above that the CMOT stage plays an irreplacable role in the parameters matching process. Luckily, the optical molasses technique can address this problem as illustrated in the following.

In this stage the 10 G/cm gradient field is turned off suddenly to zero and the trap beam detuning is further increased to -78 MHz, by which a lower equilibrium temperature can be arrived due to the polarization gradient sub-Doppler cooling process [47]. A 6 ms optimized optical molasses stage together with the CMOT enables us to achieve a denser cloud with much lower temperature and at the same time to tune the cloud center to that of the magnetic trap. In this scheme $> 95\%$ atoms of Rb in the $F = 1$ manifold with temperature ∼15 μK and density $> 10^{11}/\text{cm}^3$ can be achieved.

3.4.3 Optical Pumping

The fact that the MOT can trap the atoms in all the hyperfine states makes it necessary to purify the spins of the atoms, because only the low field seekers can be trapped as we have introduced in the magnetic trap section. In addition, the inelastic collisions between the different hyperfine states also leads to the atoms loss from the trap. All these reasons leads to another necessary process during the magnetic trap loading, i.e. the so-called optical pumping process.

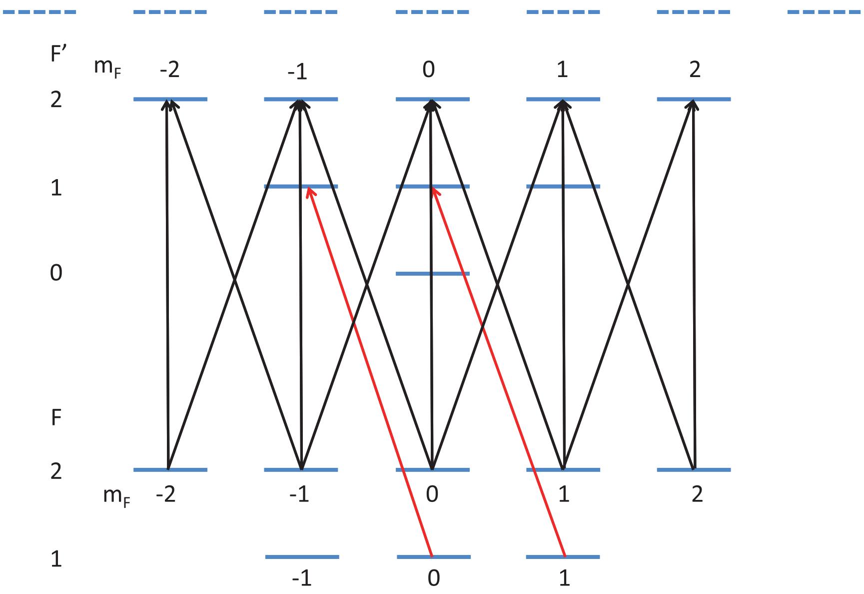

Figure 3.12: Schematic diagram of the optical pumping process for both Na and ^{87}Rb. A circular polarized optical pumping light (red line) is used to excite the σ^- transition between $F = 1$ and $F^{'} = 1$ manifold. A depump light (black line) is used to drive the $F = 2 \rightarrow F^{'} = 2$ transition so that no atoms can populate in the upper hyperfine ground state (F = 2).

In our experiment we choose this special sublevel as the $|1, -1\rangle$ state for both ^{87}Rb and Na, and the optical pumping process is achieved by choosing two different laser frequencies (a pumping light and a depumping light) for each species. The optical pumping light is a circular polarized light, which is provided by detuning the repump beam and applied to excite the σ^- transition between the $F = 1$ and $F' = 1$ manifold. The spontaneous emission of these excited states then can decay to the $F = 2$ manifold of the ground state, where the depump light is applied to excites the $F = 2 \rightarrow F' = 2$ transition. In the whole process the $|1, -1\rangle$ state appears as the only dark state where the atoms accumulate. The depumping light is obtained by detuning the trap beam. In the experiment, the detuning for both the pumping and depumping light, and the pulse duration is optimized step by step by maximizing the phase space density (PSD).

3.5 Optical Diagnostics

The trapped atoms are isolated in the ultrahigh vacuum chamber and occupy a very small space, typically on the order of 10's microns across, thus it is not feasible to measure the cloud with material probes, such as the micrometer or thermometer. The interaction between the atoms and light inspires physicists to detect this dilute gas with a resonant light relying on the dispersion or absorption, e.g. the fluorescence or absorption imaging, based on which the dynamic quantities of the cloud can be determined.

3.5.1 Fluorescence Imaging

The fluorescence signals arising from the scattering photons due to the interaction between the atoms and the resonant light as illustrated in figure 3.14(a). It is used to continuously monitor the atom number and diagnose the performance of the apparatus with a photodetector during the experiment sequence. As we know, to maximum the fluorescence signals high saturation parameter of the light beam is necessary. Thus in our experimental sequence during the detection, all the MOT beams are pulsed on at their maximum intensity. The inherent disadvantages of fluorescence imaging, i.e. the distortion of the cloud due to the imparted momentum of the photons to the atoms, the limited collection solid angle due to limited size of the aperture of the lens as well as the heating effect due to high saturation parameter of the light, are not seen as important to its performance.

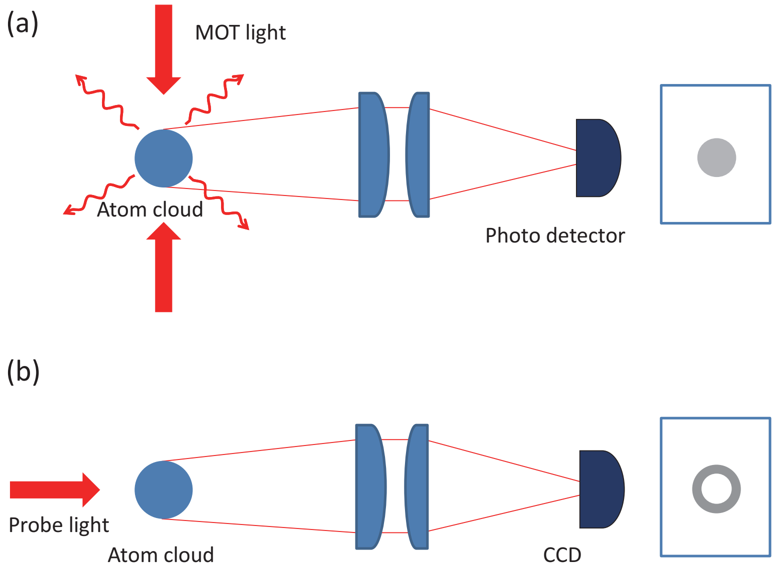

Figure 3.13: Schematic diagram of the detection process. (a) indicates the fluorescence imaging. (b) shows the absorption imaging.

3.5.2 Absorption Imaging

The absorption imaging relies on the attenuation of the incident beam intensity which is absorbed by the atoms and recorded by the CCD camera, as shown in figure 3.14(b). It works well especially with a weak probe beam and a dilute cloud sample because only under this condition the absorbed intensity of the probe beam will be linearly proportional to the cloud density. Suppose we shine a weak probe beam to a dilute cloud along z direction, the relationship between the detected beam intensity and the incident beam and the cloud density can be described by the Lambert-Beer's law as

$$\begin{aligned}\frac{dI(x,y,z)}{dz} &= -\hbar\omega R_{scatter} n(x,y,z)I(x,y,z) \\ &= \sigma n(x,y,z)I(x,y,z).\end{aligned} \tag{3.1}$$

Where, $R_{scatter}$ is the scattering rate (i.e. the collision rate), $n(x, y, z)$ is the cloud density and $I(x, y, z)$ is the probe beam intensity. The absorption cross section σ is given by Eq.(2.2) as

$$\sigma = \sigma_0 \frac{1}{1 + I/I_0 + (2\Delta/\Gamma)^2}. \tag{3.2}$$

Where, σ_0 is referred as the on resonance absorption cross section which is given by $\sigma_0 = \frac{3\lambda^2}{2\pi}$. Solving Eq.(3.1) one can obtain the beam intensity distribution inside the cloud during propagation

$$\begin{aligned}I(x,y) &= I_0(x,y)\exp^{-\sigma\int n(x,y,z)dz} \\ &\equiv I_0(x,y)\exp^{-OD}.\end{aligned} \tag{3.3}$$

Where, OD is defined by the product of the absorption cross section and the column density as $OD = \sigma \int n(x, y, z)dz$, from which one can also obtain

$$OD(x,y) = -\ln\frac{I(x,y)}{I_0(x,y)}. \tag{3.4}$$

Thus by simply measuring the intensity of the probe beam before and after passing through the cloud one can directly obtain the optical density distribution of the atoms. However, in the real case this measurement may suffer from some disturbance, such as the stray light scattering, reduction of the probe beam profile quality due to background light, noise from ambient light and camera electronics, et al. Thus, to subtract all these disturbance, except the image with and without the atoms denoted by $I(x, y)$ and $I_0(x, y)$, generally a third image is taken without both the probe light and the atoms, denoted by $I_b(x, y)$, from which a much more precision formula can be obtained

$$OD(x, y) = -\ln\frac{I(x, y) - I_b(x, y)}{I_0(x, y) - I_b(x, y)}. \tag{3.5}$$

Once the OD of the sample is known, one can obtain the physical quantities of the sample, such as the atoms number and the cloud temperature, with which all other quantities can be obtained.

Number of the Atoms

Since the OD is directly related to the column density of the cloud as introduced in the above, one can obtain the number of the atoms as

$$N = \int n(x, y, z)dxdydz = -\frac{A_{pix}}{\sigma}\sum_{pix}\ln\left(\frac{I(x, y) - I_b(x, y)}{I_0(x, y) - I_b(x, y)}\right)_{pix}. \tag{3.6}$$

Where A$_{pix}$ is the area of each pix, except the absorption cross section σ, all other quantities are in the unit of pix with each pix equal to 6 μm in our case.

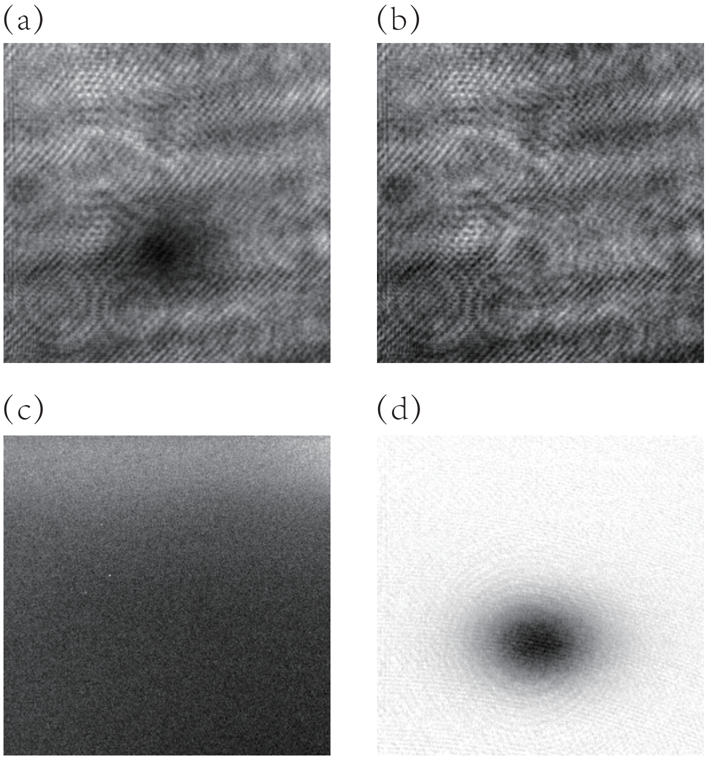

Figure 3.14: Optical density measurement with absorption imaging. (a) absorption signal with a probe light shined to the atoms. (b) the same process without atoms. (c) background imaging without both the atoms and the probe light. (d) OD of the atoms obtained according to Eq.(3.5).

Temperature of the Atoms

The ultracold temperature of the cloud is determined by measuring the momentum distribution of the atoms with time-of-flight (TOF) method, which has a Gaussian or parabolic profile above or below the transition temperature, respectively [55]. When turn off the trap and perform the TOF, the momentum distribution of the cloud can be converted to the spatial distribution, with which the temperature of the cloud along direction i (i=x, y) can be obtained

$$T_i = \frac{m(\sigma_i a_{pix})^2}{2k_B} \frac{\omega_i^2}{1 + (\omega_i t)^2}, \tag{3.7}$$

where a_{pix} is the size of a pix found by magnification measurement.

3.6 Experimental Control

The experiment involves lots of components, e.g. the power supplies, the function generators, the AOMs, the shutters, the switches, and so on, thus a precision control of the sequence and timing as well as the the corresponding communications are necessary. In our experiment all these are achieved with the popular Labview programming software in combination with a series of I/O devices as well as the general purpose interface bus (GPIB) card.

3.7 Double Species Experiments

3.7.1 A Double BEC of Na and ^{87}Rb

Following the standard step, we have already achieved a quasi pure double BEC with 5.0×10^4 (2.5×10^4) Na (Rb) atoms. A typical experimental sequence is shown in figure 3.15, and based on which a typical result is shown in figure 3.16 [1].

From figure 3.16 (a) and (b) to figure 3.16 (d) and (e) the following results can be obtained. (i) an immiscibility of the two condensates can be observed. And with the increasing of the number ratio of Rb to Na, the Na cloud will be further pushed out from the Rb cloud center, see figure 3.16 (c) and (f). The immiscibility is consistent with the theoretical prediction [85, 86]. (ii)

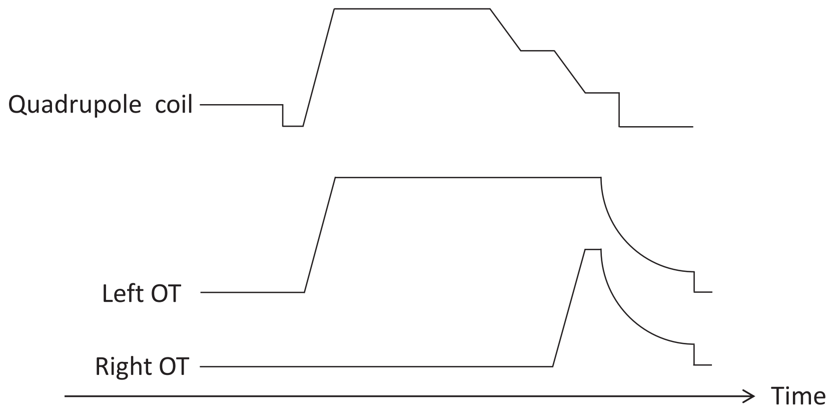

Figure 3.15: Timing diagram showing the behavior of the quadrupole coils and crossed 1070 nm optical trap.

in both the cases the Rb cloud is overlapped with the lower part of Na in the gravity direction. This separation is due to the gravitation sag and can be estimated with the final trap frequencies in the gravity direction for Rb and Na.

3.7.2 Toward Na^{87}Rb Feshbach Molecule

Nearly at the same time as the achievement of the double BEC, the Feshbach Resonances between ultracold Rb and Na atoms are observed in our lab [40]. After that our effort has been devoted to the production of ultracold Feshbach molecule. The basic idea is to sweep the B-field from above resonance position across resonance to low B-field position below resonance, see figure 3.17. Weakly bound Feshbach molecules will be formed if this process is adiabatic.

The number loss of two species at the low field position is observed, but the number recover after the dissociation process at high field did not show up. Part of the reason for this is the inadequate initial atom number of Rb

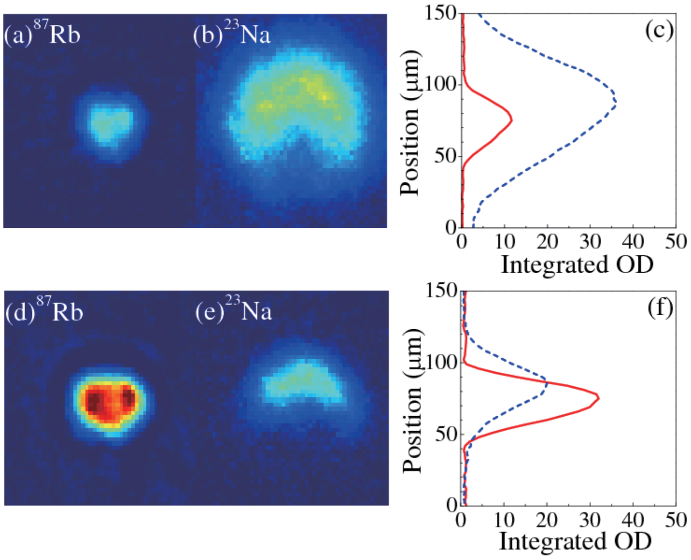

Figure 3.16: Absorption imaging of the double BEC with different atom number ratio. The upper row ((a) and (b)) has a Rb (Na) atom number of 3.5×10^3 (3.2×10^4). The below row has a Rb (Na) atom number of 8.5×10^3 (1.3×10^4). (c) and (f) is the corresponding integrated cross section, with red (blue) line for Rb (Na). Figure is from [1].

and Na. Except for the saturation vapor of Na is low at room temperature (actually 50 times lower than Rb), the trap depth for Na is only about one third of that for Rb in the crossed 1070 nm optical dipole trap. As a result, the minority Na atoms always act as the coolant in the optical dipole trap evaporation process towards higher PSD.

3.8 Conclusion

In summary, the set up of the cold atom machine is presented in this chapter, based on which the experimental results of the double BEC are described. Due to limited initial atom number of the mixture preparation, the Feshbach molecule is not observed.

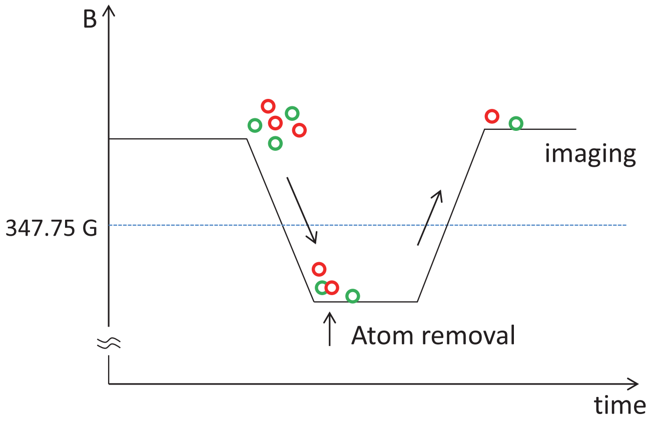

Figure 3.17: Experimental sequence for the production of the Feshbach molecules.

An important improvement for the polar molecule experiments is to increase the atom number of the ultracold mixture. In chapter 4, a multi-wavelength optical dipole trap is presented. Within this trap, the relative trap depths between Rb and Na can be tuned. As a result, a better preparation of the ultracold mixture is obtained, and based on which about 1600 Feshbach molecules are finally observed.

☐ End of Chapter.

Chapter 4

A Multi-wavelength Optical Dipole Trap

4.1 Motivation

To increase the atom numbers, we decided to introduce an additional ODT beam of very different wavelength to tune the relative trap depths of the two atoms. In this manner, we can preserve the minority Na atoms for a better condition of Feshbach molecules creation. This is possible to realize due to the fact that the two atoms have very different response to laser light and the variation of the AC polarizability vs. wavelength.

In the following, I will first give a general introduction to the basic principle of optical dipole trap for neutral atoms. These principles are then used to explain our dichotic optical trap. Then the setup of our multi-wavelength optical dipole trap will be described in detail, including the single beam 660 nm trap, the crossed 1070 nm trap, and the intensity stabilization scheme. Finally, the experimental results of this new trap will be presented.

4.2 Optical Dipole Force

4.2.1 Classical Model

An atom placed in the light field acquires an induced atomic dipole momentum $\vec{p}$ due to light electric field $\vec{E}$, with

$$\vec{p} = \alpha(\omega)\vec{E}, \tag{4.1}$$

where $\alpha(\omega)$ is the complex polarizability, which is light frequency dependent. The dipole momentum in turn interacts with the electric field and results in an interaction potential

$$\begin{aligned} U_{dipole}(x, y, z) &= -\frac{1}{2}\langle\vec{p}\cdot\vec{E}\rangle \\ &= -\frac{1}{2\epsilon_0 c}\Re(\alpha)I(x, y, z), \end{aligned} \tag{4.2}$$

where the angular bracket represents the time average of the interaction, and ϵ_0 is the vacuum permittivity. The factor $\frac{1}{2}$ is due to the reason that the dipole momentum is an induced one instead of permanent. The intensity of the light field is given by

$$I = \frac{1}{2}\epsilon_0 c|E|^2. \tag{4.3}$$

We can see from the above that the potential is proportional to the light intensity as well as the real part of the polarizability which is responsible for the dispersive part of the interaction. From Eq.(4.2) one can directly obtain the dipole force

$$\begin{aligned}\vec{F}(x,y,z)_{dipole} &= -\nabla U_{dipole}(x,y,z) \\ &= \frac{1}{2\epsilon_0 c}\Re(\alpha)\nabla I(x,y,z),\end{aligned} \tag{4.4}$$

From this, we can see clearly that the dipole force is a conservative force, and proportional to the gradient of the light field.

The absorbed power of the atoms from the light field can be obtained from Eq.(4.1) and Eq.(4.2) as

$$\begin{aligned}P_{abs} &= \langle \dot{\vec{p}} \cdot \vec{E} \rangle \\ &= \frac{\omega}{\epsilon_0 c}\Im(\alpha) I(x,y,z).\end{aligned} \tag{4.5}$$

It can also be represented in terms of the scattering rate as

$$\begin{aligned}\Gamma_{scatter} &= \frac{P_{abs}}{\hbar\omega} \\ &= \frac{1}{\hbar\epsilon_0 c}\Im(\alpha) I(x,y,z),\end{aligned} \tag{4.6}$$

which indicates that the absorption part of the interaction results from the imaginary part of the polarizability. From Eq.(4.2) and Eq.(4.6) one can see that to characterize the trapping potential for a certain wavelength, we need to determine the polarizability.

The classical Lorentz's model, which considers an electron bound to the nucleus like an oscillating elastic spring with eigenfrequency ω_0 and damping terms Γ_w corresponding to the transition frequency and scattering effect respectively, shows up as a simple and powerful tool for solving the polarizability [87]

$$\ddot{x} + \Gamma_w \dot{x} + \omega_0^2 x + \frac{e}{m_e} E(t) = 0, \tag{4.7}$$

where m_e is the mass of the electron.

Solving Eq.(4.7) with the ansatz

$$x(\omega, t) = x_0(\omega) \exp^{-i\omega t},$$

we arrive at

$$x(\omega, t) = -\frac{e\tilde{E}_0}{m_e} \frac{1}{\omega_0^2 - \omega^2 - i\Gamma_w \omega} \exp^{-i\omega t}, \tag{4.8}$$

from which the polarizability can be obtained as

$$\alpha(\omega) = \frac{e^2}{m_e} \frac{1}{\omega_0^2 - \omega^2 - i\Gamma_w \omega},$$

which can also be represented in terms of the on resonance damping rate, with relationship $\Gamma = (\frac{\omega_0}{\omega})^2 \Gamma_\omega$, as

$$\alpha(\omega) = \frac{e^2}{m_e} \frac{1}{\omega_0^2 - \omega^2 - i\frac{\omega^3}{\omega_0^2}\Gamma}. \tag{4.9}$$

Thus, the dipole potential and scattering rate in Eq.(4.2) and Eq.(4.6) can be expressed as

$$\begin{aligned} U_{dipole}(x, y, z) &= -\frac{3\pi c^2 \Gamma}{2\omega_0^3} (\frac{1}{\omega_0 - \omega} + \frac{1}{\omega_0 + \omega}) I(x, y, z), \\ \Gamma_{scatter}(x, y, z) &= \frac{3\pi c^2 \Gamma}{2\hbar \omega_0^3} (\frac{\omega}{\omega_0})^3 (\frac{1}{\omega_0 - \omega} + \frac{1}{\omega_0 + \omega})^2 I(x, y, z), \end{aligned} \tag{4.10}$$

where ω_0 corresponds to the atomic transition frequency.

In the real case the atom has a complex substructure instead of a simple two level system assumed in the above model. Generally, a more careful consideration of the dipole potential from each specific sublevel of the atom is preferred. Since the light used in the optical trap is often large detuned, the above results can be used as a good approximation. In addition, for the alkali atoms a further approximation can be made by just involving the nearest D line doublet structure, and take $\omega_0 = \frac{\omega_{D1}+2\omega_{D2}}{3}$ according to the transition strength factor for the D_1 and D_2 line. The more accurate models which considers the complex multi-level structure of the atoms will be introduced in chapter 6, where to make Na and ^{87}Rb see the same trap frequency in the optical trap, a quantum mechanical treatment for the atomic polarizability is put forward, and with which the "magic" wavelength is found.

4.2.2 Trap Characteristics

Rayleigh Range

Assume a Gaussian beam propagate along z-axis with laser output power P, the equation of the light field can be written as

$$I(x,y,z) = \frac{2P}{\pi\omega(z)^2}\exp^{-\frac{2x^2+2y^2}{\omega(z)^2}}, \tag{4.11}$$

where $\omega(z)$ is the $1/e^2$ beam radius with a propagation distance z from the Gaussian waist ω_0 ($z = 0$). The spreading of the beam profile in the free space during propagation can be precisely described by the pure diffraction theory

$$\omega(z) = \omega_0[1 + (\frac{\lambda z}{\pi\omega_0^2})^2]^{1/2}. \tag{4.12}$$

As we can see from figure 4.1 that the beam radius spreads slowly in the near-field regime and much faster or even linearly beyond a certain range, i.e. the so-called Rayleigh range, defined as the dividing line between the near-field and mid-field divergence

$$z_R = \frac{\pi\omega_0^2}{\lambda}. \tag{4.13}$$

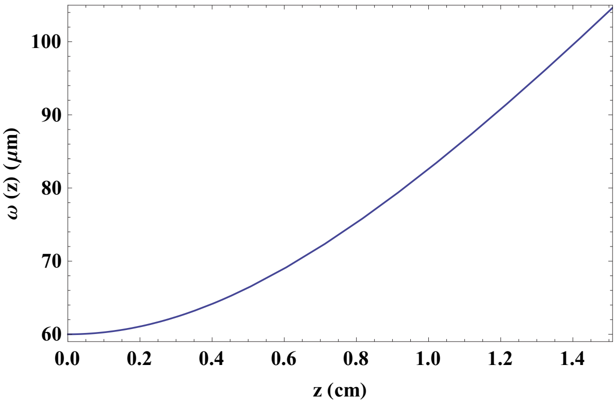

Figure 4.1: The spreading of the $1/e^2$ radius of a Gaussian beam in the free space during propagation from the waist position. The divergence angle of the beam is very small in the near-field regime, i.e. z $\leq$ 1.0 cm, and becomes almost linear when $\omega > 85$ μm. This figure is plotted by taking waist as ω_0 = 60 μm and the wavelength of the light as λ = 1070 nm.

Trap Depth

The optical potential can also be written as

$$U_{dipole}(x, y, z) = U_0 \exp^{-\frac{2x^2+2y^2}{\omega(z)^2}}, \tag{4.14}$$

where U_0 is denoted as the trap depth, determined by Eq.(4.10) and Eq.(4.11), and related to the light frequency and the beam intensity for a given trap size. To reduce the scattering rate while keeping the same trap depth, one can further increase the detuning at the cost of higher laser power.

Trap Frequency

The trap frequency can be obtained by applying the harmonic approximation to the dipole potential when the temperature of the atoms is much smaller than the trap depth

$$f_i = -[\frac{1}{2\pi m}\frac{\partial^2 U(x,y,z)}{\partial i^2}]^{1/2}_{x=y=z=0}, \tag{4.15}$$

where $i = x, y, z$, and m is the mass of the atom.

Taking the single beam case as an example, under the harmonic approximation the trap potential can be written as

$$U_{dipole}(x,y,z) = \frac{1}{2}m(\omega_x^2 + \omega_y^2 + \omega_z^2). \tag{4.16}$$

Substitute Eq(4.16) into Eq(4.15), the trap frequency in the radial and axial direction can be obtained as

$$\begin{aligned} \omega_x = \omega_y &= \sqrt{\frac{4U_0}{m\omega_0^2}}, \\ \omega_z &= \sqrt{\frac{2U_0}{mz_R^2}}. \end{aligned} \tag{4.17}$$

Since z_R is much larger than ω_0, the trap frequency in the radial direction is much larger than that in the axial direction.

Gravitational Sag

The dipole trap potential includes the gravitation's contribution in the laboratory frame can be written as

$$U_{total}(x, y, z) = U_{dipole}(x, y, z) + mgy. \tag{4.18}$$

From which the gravitational sag can be obtained in the harmonic approximation

$$y = -\frac{g}{\omega_y^2}, \tag{4.19}$$

where g is the gravitational constant and ω_y is the trap frequency in the y direction.

The gravitation not only breaks the geometric symmetries of the trap potential, see figure 4.3 and figure 4.2, but also leads to a displacement between the two cloud center for the samples with different trap frequencies in the y direction. On the other hand, the gravitational sag relates to trap only by the trap frequency, thus it can be canceled with a "magical wavelength" trap in which the dual species has the same trap frequency, see chapter 6.

In summary, the optical dipole force is a conservative force which arises from the interaction between the electric field induced atomic dipole momentum and the far-detuned light field gradient [88, 89, 90, 87]. The dispersive part of the interaction with a spatial dependent light intensity distribution results in a spatial varying energy shift, i.e. the so-called AC-Stark shift [91]. For a red detuned laser light, the energy shift is negative and the potential minimum can be found at the intensity maximum position. The atoms are therefore attracted into the light field. For a blue detuned light, it is positive and the atoms are forced out of the trap. The absorptive part of the interaction leads to the heating of the atoms thus sets the limit of the performance of the trap. However, from Eq(4.10) $\Gamma_{scatter} \propto \frac{1}{\Delta^2}$ and $U_{dipole} \propto \frac{1}{\Delta}$, generally with a large detuning the scattering process can be neglected.

4.3 The Idea of A Multi-wavelength Trap

In figure 4.2 we show a multi-wavelength optical trap which is made up of a single 660 nm beam and two crossed 1070 nm beams. Compare with single color 1070 nm trap, see figure 4.3, one can see that with the help of the 660 nm light the trap depth for Na has been greatly increased. With higher power of the 660 nm light the trap depth for Na can be even much larger than that for Rb, which indicates the tunability of the relative trap depths between Rb and Na during the evaporation.

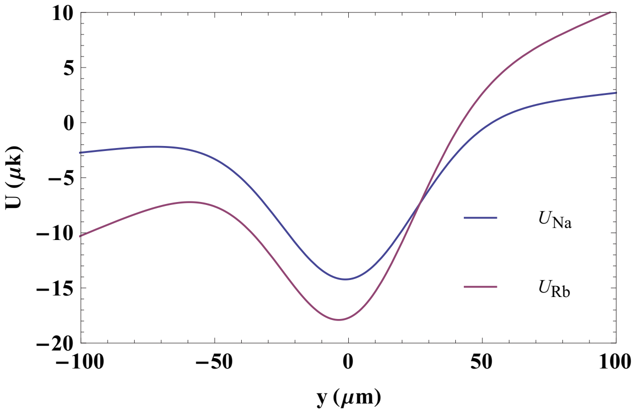

Figure 4.2: Profile of the multi-wavelength optical trap for ^{87}Rb and Na along the vertical direction. It is formed by the superposition of the crossed 1070 nm trap and the single beam 660 nm beam focused at the trap center. The two arms of the 1070 nm trap have a beam waist of 48 μm and 53 μm and power of 309.8 mW and 314 mW. The 660 nm beam has a beam waist of 50 μm and power of 133.75 mW. The effective trap depth for ^{87}Rb and Na is 12.03 μK and 10.69 μK, respectively.

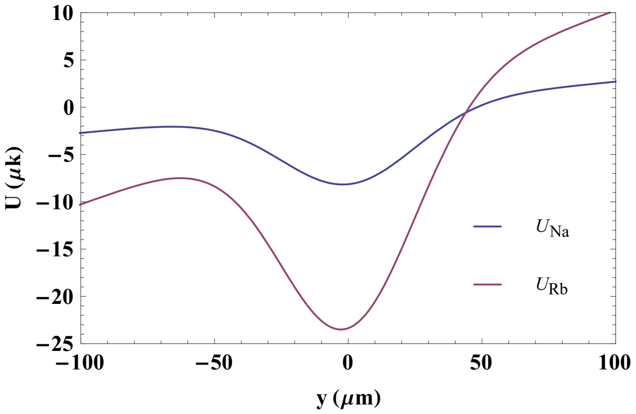

Figure 4.3: Profile of the 1070 nm crossed optical dipole trap for ^{87}Rb and Na along the vertical direction. The trap parameters are the same as that in figure 4.2, with which the effective trap depth for ^{87}Rb and Na is 16 μK and 6.107 μK.

4.4 Setup of the Multi-wavelength Optical Trap

The multi-wavelength optical trap is a superposition of the crossed 1070 nm trap and a single 660 nm beam focused at the 1070 nm trap center, see figure 4.4. Due to the optical access limitation set by the four MOT beams, imaging lights and optical pumping lights for both Rb and Na, and the microwave horn antenna, the 660 nm beam is almost overlapped with one of the 1070 nm beams. To avoid possible damage to the 1070 laser, the 660 nm beam is tuned with a small angle ($< 5^\circ$) away from the incident 1070 nm light direction. In the following section we will illustrate the optical setup of the 1070 nm dipole trap and the 660 nm dipole trap respectively.

4.4.1 1070 nm Optical Dipole Trap

The 1070 nm optical dipole trap is based on the linear polarized fiber laser (IPG Photonics) which has a single output mode with power up to ~100 W and a nice Gaussian beam quality ($M^2 < 1.05$). The output power of the

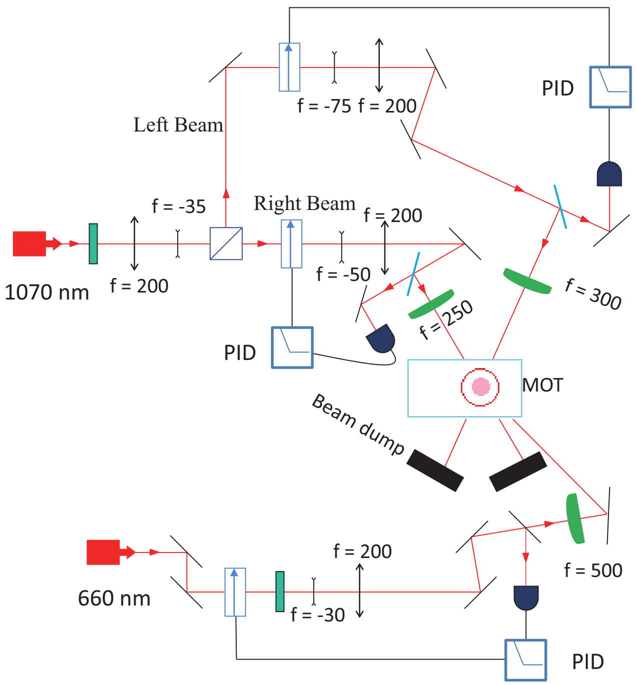

Figure 4.4: Optical layout of the multiwavelength optical dipole trap. For the 1070 nm trap, a $\lambda/2$ plate and a PBS is used to divide the laser beam into two arms to achieve individual control of the two beams, with nicknames “left” beam and “right” beam. The the 660 nm single beam is shined to the atoms from the opposite side of the glass cell, with a small anger to the “right” beam to avoid possible damage to the laser. In both cases, the AOM is used as an optical switch as well as part of laser intensity stabilization scheme.

laser is divided into two arms with the help of a $\lambda/2$ plate and a polarizing beamsplitter (PBS) cube, see figure 4.4. After that each of the two beams is then sent to a 110 MHz AOM (Crystal Technology) which not only works as an optical switch but also works for the intensity stabilization. The last step then is to choose the “right” optical lenses to focus the two beams down to $\sim 50\ \mu$m while keeping perfect Gaussian profile.

Crossed Beam Configuration

The crossed beam configuration is achieved by passing the two focused arms of the 1070 nm beams into the glass cell individually and then cross each other at the atom's position with an angle of 62°, as shown in figure 4.4.

First the laser beam size is designed to shrink by ∼6 times with a pair of planoconvex-planoconcave lens (f = 200, -35 mm) to enable it to pass through the AOM with a high working efficiency. Then according to

$$\omega_F = \frac{\lambda f}{\pi \omega_L}, \tag{4.20}$$

where ω_F is the spot radius of the focus, ω_L is the radius of the collimated beam at the lens. To ensure a focus of ∼50 μm with the final lens, the laser beams of the two arms are then expanded respectively. Generally, to preserve the nice Gaussian profile and to ensure good pointing stability, the least number of optical elements should be used in the setup.

Trap Size and Profile

In our setup both the two arms of the 1070 nm optical trap are designed with a beam waist of ∼50 μm in the focus, which provides an effective trap depth of ∼50 μK for Rb and ∼18 μK for Na with only 0.8 W power in each beam. This is achieved by making the optical elements working in the diffraction limit with numerical aperture (NA) matched lens group and spot radius. Due to the optical access limititation, the final lens is chosen to be f = 300 (250) mm (Achromatic Doublet) for the "left" ("right") beam. The spot radius of the "left" ("right") beam is magnified by 4 (∼3) times before projected onto the final lens. The beam profile is then measured with a Mightex CCD camera (SCE-B013-U) and fitted with Gaussian beam equations in the Rayleigh region. The measured result is shown in figure 4.5, which gives a beam waist of 52 (47) μm and 63 (55) μm for the “right” (“left”) beam in the horizontal and vertical direction respectively. This is close to the designed size. The difference of the waists between the horizontal and vertical direction for both the two arms mainly comes from optical aberration caused by the optical elements, such as the lens.

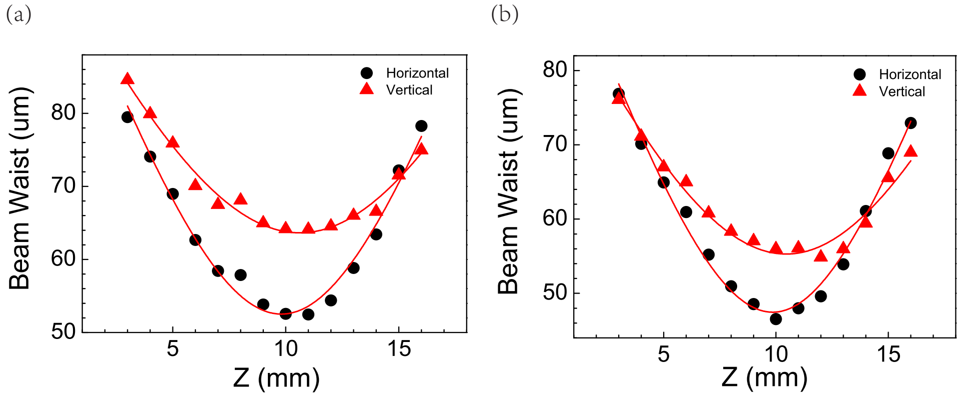

Figure 4.5: Beam profile of the crossed 1070 nm optical trap along the beam propagation direction, i.e. the z-axis direction in our lab frame. (a) and (b) refers to the beam profile measured with a Mightex CCD camera (SCE-B013-U) both in the horizontal (black) and vertical direction (red) for the “right” and “left” beam respectively, as indicated in figure 4.4. The beam waist is fitted with Eq.(4.12), which gives the beam waist of the “right” (“left”) beam as 52 (47) μm and 63 (55) μm in the horizontal and vertical direction respectively.

4.4.2 660 nm Optical Dipole Trap

The 660 nm optical trap is based on a linear polarized Cobolt Flamenco^{TM} diode-pumped solid-state (DPSS) laser with maximum output power of 500 mW. Before put this laser into the trap, the initial condition of the laser is measured. Figure 4.6 shows the beam intensity distribution of the laser and

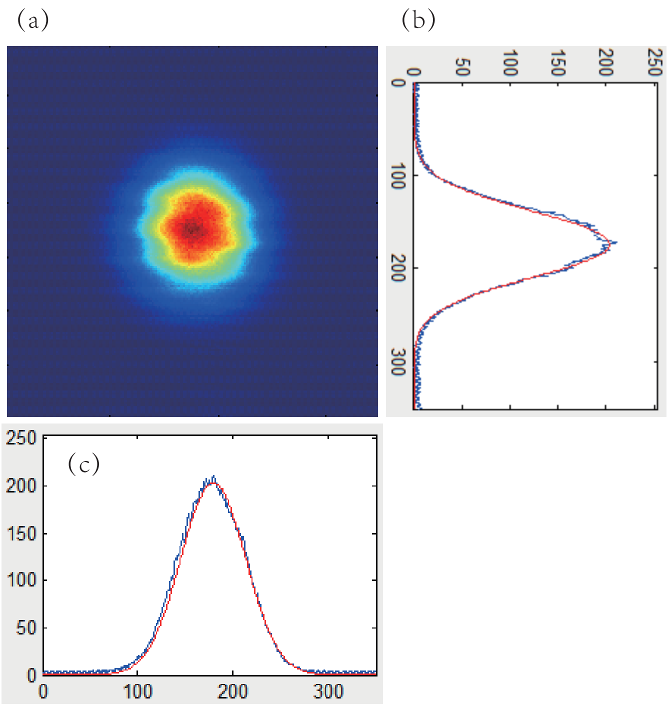

Figure 4.6: Typical profile of the 660 nm laser beam measured close to the output end. (a) is the beam intensity distribution measured directly by shining the laser onto a Mightex CCD camera (SCE-B013-U). The wrinkled structure coming from the interference effect from the neutral density filters used in front of the CCD chip. (b) and (c) shows the profile of the intensity distribution (blue line) and the Gaussian fitting (red line) in the vertical and horizontal direction respectively.

the Gaussian fitting of the beam profiles both in the vertical and horizontal direction, which suggests that the beam quality of the laser already satisfies the requirement for an optical trap. In figure 4.7 the spot radius of the laser beam is also measured and fitted with Eq.4.12 in the propagation direction, which gives a spot radius of ~362 μm and ~374 μm in the horizontal and vertical direction respectively. With the measured spot radius of the beam and fix the final lens as f = 500 mm, one can then chose the lens group to achieve the desired beam waist with help of the Zemax program.

As a typical example, we illustrate a typical scheme that by expanding

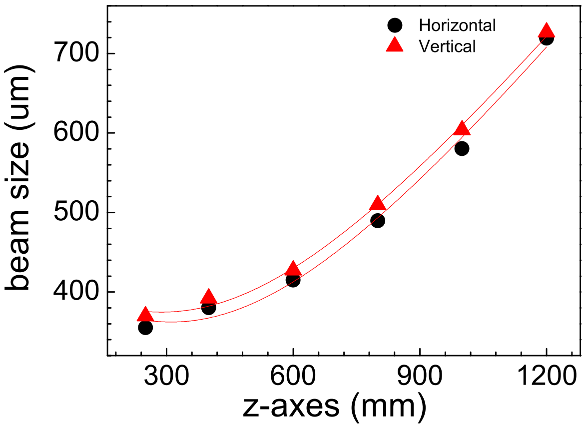

Figure 4.7: Test of the spot radius of the 660 nm laser, which is performed by measuring beam profile at different distances from the output end of the laser, and then get it fitted with the formula that describing the propagation of a Gaussian beam in the free space, i.e. Eq.(4.12). The result gives a spot radius of ∼362 μm and ∼374 μm and a M^2 factor of ∼1.2 and ∼1.18 in the horizontal and vertical direction respectively. This information is of significant importance for one to design the setup of an optical trap with this laser which will be shown later.

the beam radius by 6 times with a pair of lens (f = -50, 300 mm), we are able to achieve a beam waist of ∼25 μm and ∼23 μm at the focus of the final lens (f = 300 mm) with nice Gaussian profile in both the horizontal and vertical direction, see figure 4.8. The difference of the waist by 2 μm as well as the focus by 0.5 μm between the two directions is derived from the error of the measurement and can be eliminated with more careful treatment.

In the multi-wavelength trap, to keep the trap size as that of the 1070 nm trap we just design the beam waist around 50 μm. This is achieved by expanding the spot radius with a pair of lens (f = -30, 200 mm) before shined to the final lens (f = 500 mm). The measured beam waists match well with the Zemax program modeling results, which also promises a nice Gaussian profile from another point of view besides the direct Gaussian fitting.

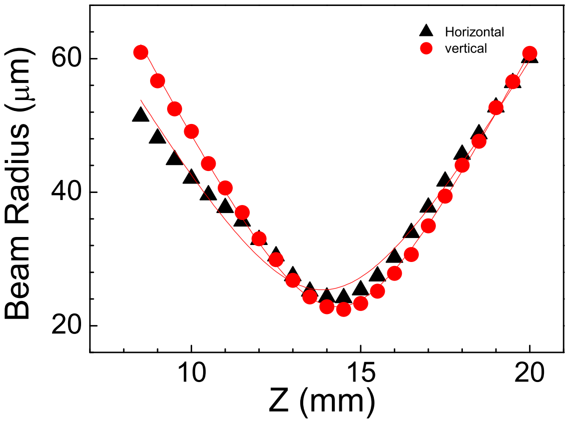

Figure 4.8: Typical beam profile of 660 nm trap along the beam propagation direction. With a beam expander (f = -50, 300 mm) before projected onto the final lens (f = 300 mm) the beam can be focused down to ~25 μm and ~23 μm in both the horizontal and vertical direction. The measurement method is the same as we used to test the profile of the 1070 nm trap in figure 4.5.

4.4.3 AOM driver

The AOM is an essential part in the setup of an optical trap as we can see from the above sections. In brief one can take it as a frequency shifter based on the Brag Diffraction principle with the efficiency of the first order beam proportional to the acoustic power and inversely proportional to the square of the light wavelength. For more detailed description of the principle and working parameters one can see [92, 93] and reference therein. In our case, no matter in the setup of the 1070 nm trap with a 110 MHz AOM (Crystal Technology) or in the 660 nm trap or 946 nm trap (in chapter 7) with a 80 MHz AOM (Gooch & Housego) a high power RF driver is needed for the AOM to achieve the highest diffraction efficiency. The schematic diagram of the AOM driver is illustrated in figure 4.9 and the detailed electronic circuit

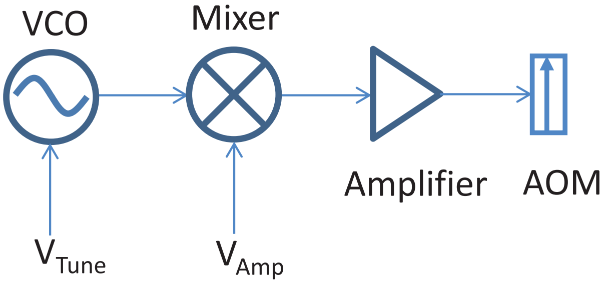

Figure 4.9: Schematic diagram of the AOM driver. The RF frequency fed to the AOM is control by the voltage controlled oscillator (VCO) with a tuning DC voltage V_{Tune}, and the power of the RF signal is controlled by the mixer with another DC voltage V_{Amp}.

can be found in appendix B.1. The RF signal is produced by a voltage controlled oscillator with amplitude can be controlled by a DC voltage V_{Amp} sent to the mixer, which is then sent to an amplifier before fed to the AOM.

Figure 4.10: The real picture of the box which contains the circuits for both the AOM driver and the intensity stabilization.

4.4.4 Intensity Stabilization

The laser intensity stabilization is also an essential part in the setup of an optical trap due to the following reasons. First of all, one needs to vary the beam intensity by up to two orders of magnitude in the evaporation process, however the beam intensity is not necessary linearly related to the power of the RF signal in the AOM driver. On the other hand, the low frequency noise inside the laser beam may lead to the heating effect on the atoms and the subsequent atom loss in the optical trap. Additionally, and perhaps more importantly, the unstable laser power may cause a misunderstanding of the trap, especially for the one involves an optical fiber where the power fluctuation can even reach $\sim$5%.

The intensity stabilization has been involved in the setup of our optical trap, see figure 4.4, with the detailed electronic circuit in appendix B.2. The backside polished mirrors in the 1070 nm trap or the special mirror with high transmission and low reflection in the 660 nm trap enables one to couple a small fraction of the laser light into a photodetector so that the light signal can be transformed into a voltage signal and then compared with a reference voltage sent by the computer. The error signal is sent to a proportional-integral-derivative controller (PID), where it is rectified before delivered to the AOM driver to increase or decrease the diffraction efficiency of the AOM until it is zeroed in, hence the desired beam intensity.

Laser Intensity Calibration

With the intensity stabilization added in, besides the stabilized laser power one can also enable the control of the laser power with a linear relationship to the reference voltage sent by the computer, see figure 4.11 and figure 4.12, which makes it much more convenient to control the evaporation process, e.g.

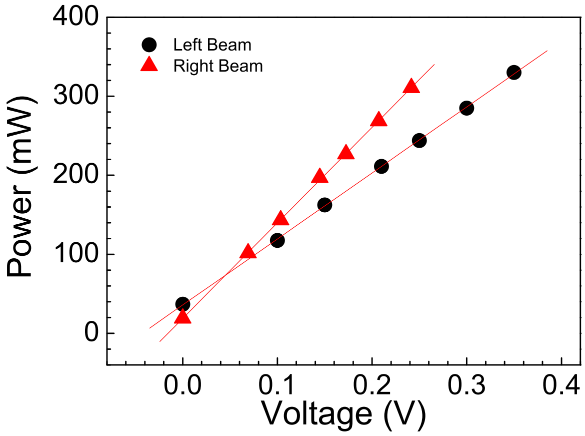

Figure 4.11: Calibration of the scaling relationship between the power of 1070 nm beams and the reference voltage output from the computer. The linear relationship between the laser power shined to the atoms and the output reference voltage enables us a good control of the trap depth during the optical loading process as well as the evaporation process.

the evaporation rate in each beam at different stages. One consideration is that all the photodetectors in the servo are placed before the glass cell, this is to avoid possible misalignment when optimizing the crossed 1070 nm trap and the alignment of the 660 nm trap.

4.4.5 Optical Alignment

Alignment of the 1070 nm trap

The 1070 nm trap is displaced horizontally from the magnetic trap center. This is mainly to suppress the Majorana loss in the forced evaporation process in the magnetic trap. The optimization of the 1070 nm trap position is performed by maximizing the PSD of both Rb and Na, which gives a displacement of 75 μm from the magnetic trap center. This is consistence with

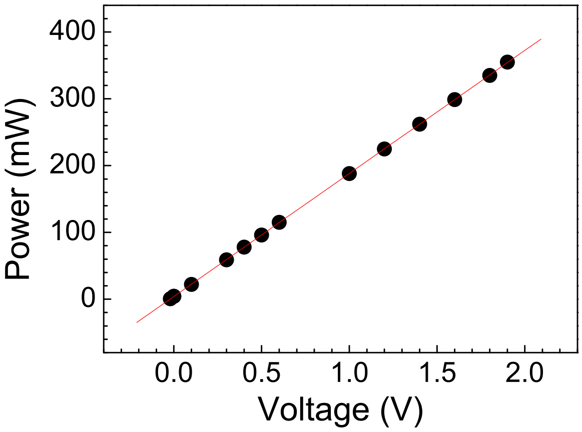

Figure 4.12: Calibration of the scaling relationship between the 660 nm laser power and the reference voltage given by the computer. The linear relationship appears pretty similar to that of the 1070 nm trap, which provides a great convenience for us to tune the trap depth for Rb and Na together with the 1070 nm beams in the multi-wavelength optical trap.

the theoretical prediction. In addition, it has been confirmed that compared with the configuration with the optical trap center located right below the magnetic trap, this configuration can provide a much higher wall thus more efficient to suppress the Majorana loss [1, 56].

Alignment of the 660 nm trap

The alignment of the 660 nm trap center to that of the 1070 nm trap can be divided into two steps. The first step is to adjust the optical path toward the MOT center with help of a weak trapping light of Rb. A good alignment results in a quick decreasing of the fluorescent signal detected by the camera. Then optical path direction can be fixed by two iris diaphragms, and the final lens and the backside polished mirror is added in the optical path. By just maximizing the output power of the 660 nm beam from the small slit of the

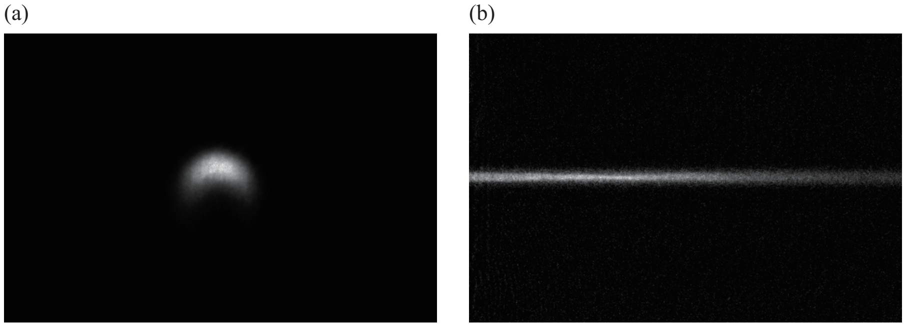

Figure 4.13: Alignment of the 660 nm trap center to that of the 1070 nm trap. (a) shows the alignment in the horizontal direction with help of Rb thermal cloud, where a good overlap results in symmetrical distribution of the blown cloud. (b) indicates the alignment in the vertical direction with Na atoms. By just loading the Na thermal cloud into the 660 nm trap or the 1070 nm trap, and compare the fitted vertical positions of the Na thermal cloud in the trap, one can directly judge the alignment.

two iris diaphragms, the fine alignment can then be performed with help of both the Rb atoms and Na atoms. To make the 660 nm beam "right" passing through the 1070 nm trap center, a in trap absorption image is applied. A good alignment in the horizontal direction arising with a symmetrical distribution of the blown Rb thermal cloud, as shown in figure 4.13 (a). The alignment in the vertical direction is done by just loading the thermal Na atoms into the crossed 1070 nm trap and the 660 nm trap respectively, and then compare the fitted cloud center in the vertical direction, see figure 4.13 (b).

To achieve a good overlap between the 1070 nm trap center and the focus of the 660 nm beam, a manual translation stage for the final lens is suggested. In our case with beam waist of 50 μm the 660 nm trap has a Rayleigh length of 12 mm according to Eq.(4.13), which makes it convenient to tune the overlap manually.

4.5 Experimental Results

4.5.1 Improvement for Double BECs

The 660 nm trap is applied during the optical trap loading process right after the forced microwave evaporation stops at 6833.8 MHz in the quadrupole trap, which deepens the trap depth for Na while still keeps a relative large trap depth for Rb. Thus, a larger number of the Na atoms can be loaded into the optical trap. In fact we have observed an increase of the Na atom number by ∼23% compared with the case without the 660 nm trap from a statistics for several days. In addition, the cloud of both Rb and Na has a higher peak and smaller size compared with the case without the application of the 660 nm trap in the loading process. This is attributed to the lowered trap depth for Rb thus the colder Rb cloud and subsequent the colder Na atoms, because the coolant role of the Rb atoms and the Na atoms are sympathetic cooled.

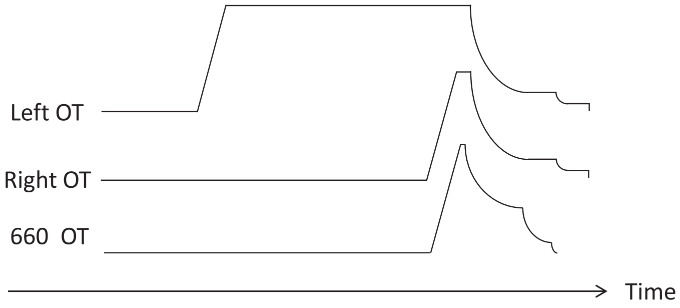

Figure 4.14: Timing of the evaporation process in the multi-wavelength optical trap.

Right after the thermal mixture of Rb ($\sim 7.4\times10^5$) and Na ($\sim 3.5\times10^5$) has been loaded into the two-color optical trap, the evaporation process is performed. At the beginning, the Rb atoms are colder than the Na atoms thus continue working as the coolant. With the same evaporation rate of the three beams, see figure 4.14, and nearly the same trap depth for the two clouds, the Na atoms get colder much faster than the Rb atoms.

In fact, at trap depth 19 μK (20 μK) for Na (Rb) with atom number 3.4×10^5 (4.5×10^5) and calculated PSD 0.63 (0.18), we found that the temperature of Na is already lower than Rb ($T_{Na} : T_{Rb} \approx 0.85$). In the subsequent evaporation, the Na atoms act as the coolant instead of the Rb atoms, thus the BEC phase transition of the Na atoms comes out first with the Rb atoms lagged behind.

At position of trap depth 6.5 μK for Na and 5.5 μK for Rb we obtain a quasi-pure of BEC of Na with atom number 2.4×10^5 and thermal Rb cloud with atom number 1.4×10^5 and calculated PSD of 0.4. Further cooling results in a pure double BEC with Na atom number 1.5×10^5 and Rb number 1.0×10^5. We point out that the removal of the 660 nm trap is necessary due to the reason that the red detuned light contributes to the trap frequency for an atom while the blue detuned one reduces it. Thus, the 660 nm light will further increase the trap frequency ratio ω_{Na}/ω_{Rb}, and as a result, worsen the overlap of the cloud center of Rb and Na due to the gravitational sag.

In figure 4.15, the evaporation trajectory of the thermal mixture toward BEC phase transition is shown, which gives a evaporation efficiency, defined by $\alpha = -\frac{log(\rho/\rho_0)}{log(N/N_0)}$, of 1.27 for Rb. The PSD of Na increases much faster than that of Rb, which means Na works as the coolant and Rb is sympathetically cooled in the final stage.

In summary, with the help of the multi-wavelength optical trap the atom number of the double BEC has been increased by three times. The added 660 nm trap enables us the tunability of the relative trap depths between Na and Rb in the evaporation process. This results in the swapping of the

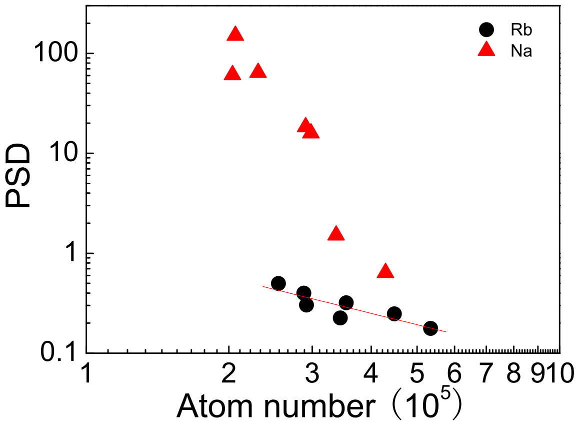

Figure 4.15: Evaporation trajectory of Na and Rb in the optical trap, which gives a evaporation efficiency of 1.27 for Rb. The PSD of Na increases much faster then that of Rb, which indicates the coolant role of Na at the final stage.

coolant role from Na to Rb, and the minority Na atoms can be preserved.

4.5.2 Observation of the Feshbach Molecules

The formation of the Feshbach molecules of Na^{87}Rb prefers a very low temperature, even very close to the BEC phase transition. This requires an ultracold preparation of the mixture with a large atom number for both Na and Rb. Where an intrinsic contradiction arises. The added 660 nm trap can increase the atom number of the double BECs, meanwhile, it also increases the trap frequency ratio between Na and Rb. Additionally, since the BEC transition temperature of the atoms in a 3-D harmonic trap is directly related to the atom number by $k_bT_c \approx 0.94\hbar\bar{\omega}\varpi N^{1/3}$ [73]. It's hard to obtain a large ultracold mixture with temperature very close to the critical temperature. Thus, in the experiment a tradeoff between the atoms number and the separation of the cloud center as well as the temperature of the cloud is necessary.

Experimentally, a thermal mixture of Na and Rb with measured temperature of ∼ 540 nK and ∼ 460 nK has been achieved, see figure 4.16. The thermal cloud of Na (Rb) has an atom number of 1×10^5 (1×10^5), cloud size of 4.2 μm (7.5 μm) in the y direction(i.e. the gravitation direction), peak density of 1.4 $\times10^{13}$ cm^{-3} (1.86 $\times10^{13}$ cm^{-3}) and a calculated PSD of 2.3 (0.4). According to Eq.(4.19) the calculated displacement between the two cloud center is ∼4.4 μm.

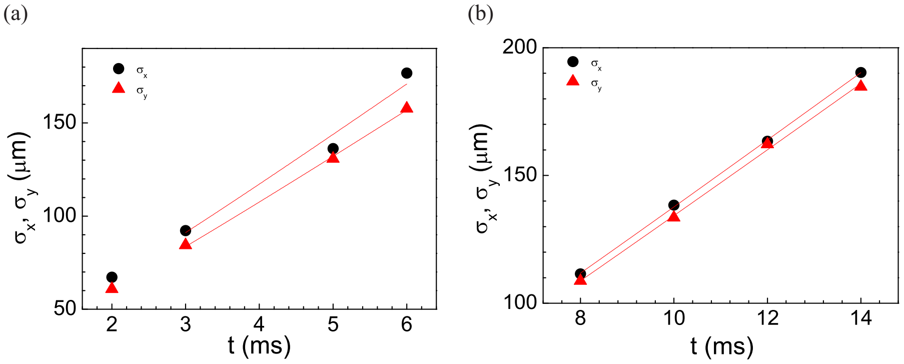

Figure 4.16: Temperature of the thermal mixture determined by the time of flight (TOF) method. (a) and (b) indicates the $1/e^2$ size of the Na and the Rb atomic cloud measured with different evolution time. The fitted result gives the temperature of the Na atoms ∼540 nK and the Rb atoms ∼460 nK.

Molecule Signals

With the improved experimental condition, we observed around 8000 atoms recover of the Na atoms by sweeping the magnetic field adiabatically from 349.6 G across the resonance position (347.75 G) downward to 347.1 G at a constant rate, and then sweeping the magnetic field back to 349.6 G without any holding. A typical result is shown in figure 4.17. The atom

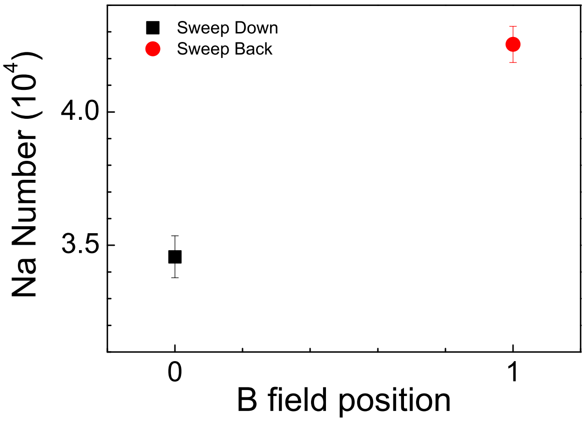

Figure 4.17: Atom number recovery of Na. Position 0 indicates the sweeping down process in which the B-field is swept from 349.58 G across the resonance (347.75 G) down to 347.12 G, and position 1 corresponding to the sweeping back process in which the B-field is swept back to 348.56 G after swept down. The two processes give a number difference of ∼8000. The experimental condition Na (Rb) is N = 4.3 × 10^4 (1.2 × 10^5).

number difference between the sweeping down and sweeping back process has a suggestion of the formation of Feshbach molecules.

To have it verified, the separation of molecules from the atom cloud is achieved by utilizing the different magnetic momentums between the two species. Right after the sweeping the B-field down to 347.1 G, a B-field gradient is applied. The Stern-Gerlach effect then results in a totally separation of the residual atoms and the weakly bound molecules [31, 32]. By inversing the association process, i.e. dissociating the molecules by sweeping the B-field from 347.1 G across the resonance 347.75 G to 349.6 G, and then detecting the atom number we still obtained ∼1600 molecules.

A typical result is shown in figure 4.18. By sweeping the B-field from 349.6 G to different end with the same sweeping rate and detecting the atom

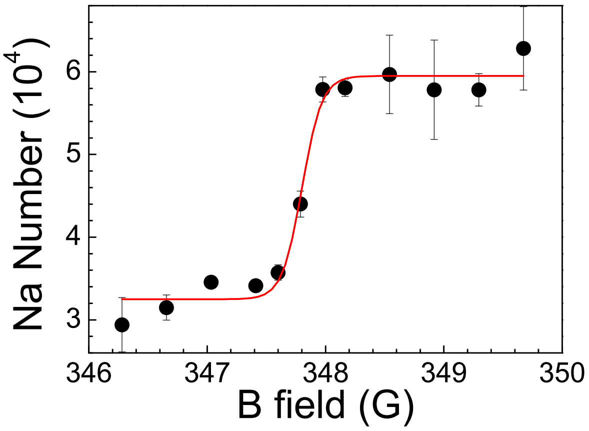

Figure 4.18: Relationship between the atom number of the Na and the final B-field position. The data is fitted with a hyperbolic tangent function [2], which gives the resonance position of 347.80 G and width of 0.19 G.

number of Na, the molecule signal is verified. A hyperbolic tangent function fitting of the data gives the resonance of 347.80 G with width 0.19 G.

□ End of Chapter.

Chapter 5

Laser System for High Field Imaging

5.1 Background and Motivation

For polar molecule experiment, the capability to detect molecules at high field is important. Due to the inductance of the coils, the switching off of a big B-field takes ∼100 μs and another ∼20 ms is also needed until the magnetic field become stable. This sets an impediment for the detection of the molecules at low, or even zero, B-field. In addition, during the magneto-association process the weakly bound Na^{87}Rb Feshbach molecules are immersed in the atom bath. Thus a quick removal of the atoms from the molecules is required to avoid inelastic collisions with these atoms [94].

The resonant wavelengths of both the Rb and the Na are shifted by the external magnetic field, which make the cooling and trapping light unable to image or remove the atoms. Thus a "new" laser light is necessary.

In this chapter first the Zeeman shift of the excited states (for ground state see section 2.1) of both ^{87}Rb and Na atoms in the magnetic field will be calculated. Then the high field imaging system will be introduced, as an example, we will have a detailed description of the setup for Rb. At last, the experimental result will be presented.

5.2 Zeeman Shift of the Excited States

For the excited state, the Hamiltonian contains the hyperfine splitting and the B-field induced energy shift can be written as [95]

$$H = \frac{A_{hfs}G}{\hbar^2} + B_{hfs}\frac{3G^2 + \frac{3}{2}G - I(I+1)J(J+1)}{2I(2I-1)J(2J-1)} + \frac{\mu_B B}{\hbar}(g_J Jz + g_I I_z), \tag{5.1}$$

where

$$G = I_x \otimes J_x + I_y \otimes J_y + I_z \otimes J_z,$$

and μ_B is the Bohr magneton, A_{hfs} and B_{hfs} is the magnetic dipole constant and electric quadrupole constant respectively.

Via the diagonalization of the above Hamiltonian with the Mathematical program, the exact energy shift of the D_2 line of ^{87}Rb and Na is obtained respectively, as shown in figure 5.1 and figure 5.2. For the $|3,3\rangle$ state, a energy shift of ~975.5 (974.1) MHz for ^{87}Rb (Na) is obtained at 348 G. From the Breit-Rabi formula, the energy shift of the ground $|2,2\rangle$ state is ~487.7 (487.0) MHz for ^{87}Rb (Na) at the same B-field. Thus a frequency shift of 487.8 (487.1) MHz for the Rb (Na) probe beam is needed, compared with that at zero B-field. In addition, the capability of the high field imaging at other B-field, e.g. 487 G, requires a large tuning range of the laser frequency. It is based on the all these considerations that a new laser system is built.

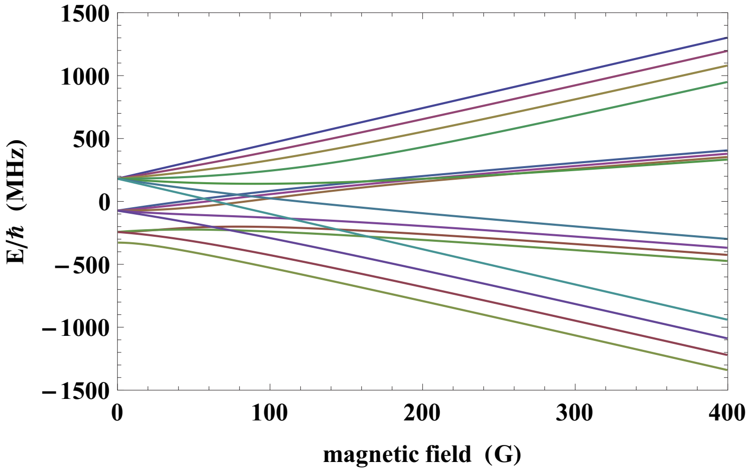

Figure 5.1: Hyperfine structure of the D_2 line of ^{87}Rb in the external magnetic field. The sublevels are grouped by the value of quantum number F (F = 3, 2, 1, and 0, from the top to the bottom) in the low field regime and m_J (m_J = 3/2, 1/2, -1/2 and -3/2) in the strong field regime.

5.3 High Field Imaging System

The center part of the high field imaging system is the distributed feedback (DFB) laser with frequency locked to the trap laser via the offset locking scheme, which allows a wide tunability of the laser frequency as well as a large capture range with long term stability.

5.3.1 DFB Laser

A photo of the DFB laser is shown in figure 5.3. The chip is from Eagleyard with an integrated grating structure. It is mounted with a cage plate mount (Thorlabs CP04) and placed in an air-tight aluminum case. The diode has a build-in TEC which is controlled by a Thorlabs temperature controller (Thorlabs TED 200C). The current driver is the same as we have used in the ECDL. The output beam is collimated with an aspheric lens (C230TME-B). Compared with the ECDL, a big advantage of the DFB laser is its large

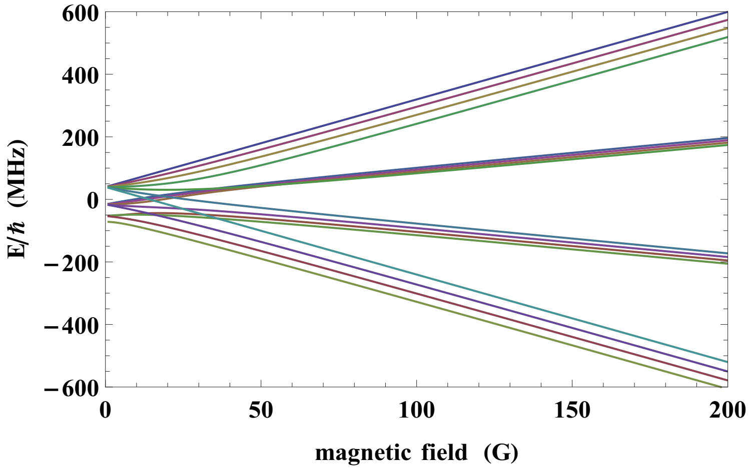

Figure 5.2: Hyperfine structure of the D_2 line of Na in the external magnetic field. The sublevels are grouped by the same way as that of the D_2 line of ^{87}Rb with the only difference being the dividing line between the low field and the strong field regime.

mode-hop range. Several hundred GHz can be covered smoothly with the combined temperate and current tuning.

5.3.2 Frequency Offset Locking Scheme

The offset locking of a laser to a reference laser is based on measuring and controlling the beat note between these two lasers [96]. The reference laser (the trap laser for Rb laser cooling) beam and the free running DFB laser beam are superimposed on a PBS with each beam of ∼100 μW power. The beat note $\Delta f = f_{DFB} - f_{trap}$ (619.8 MHz) is measured by a fast photodetector (EOT ET-2030A) and subsequently divided by 4 times with a frequency divider (RFBay FPS-4-13). The RF signal is then mixed (Mini Circuits ZFM-3-S+) with the output of a VCO (Mini Circuits ZX95-310A-S+). This is followed by a low pass filter (Mini Circuits BLP-50+) to extract the $\Delta f - f_{VCO}$ part of the signal only. This signal is then divided into two equal

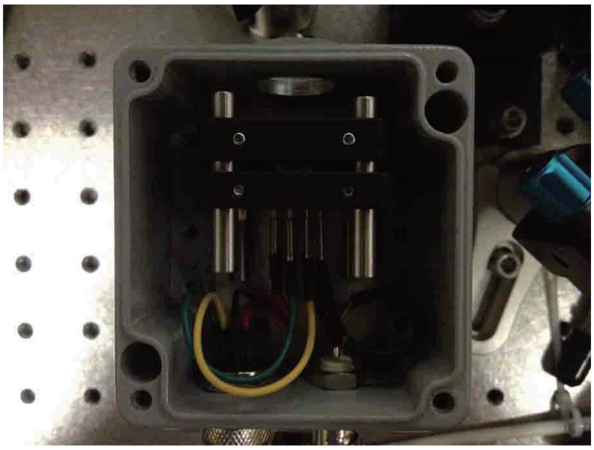

Figure 5.3: A photo shows the inner setup of the DFB laser.

branches. A 1-meter long coaxial-cable is used to impart a phase shift to one of the branches before they are recombined with a phase detector (Mini Circuits ZX95-100-S+). The output signal after a second low pass filter then gives the error signal.

The schematic diagram of the above process is illustrated in figure 5.5, and a photo of the setup is shown in figure 5.6. From figure 5.7, we can see that the error signal varies with the beat note frequency, where the zero crossings of the signal provide the locking points for the DFB laser with a servo loop. The electronic circuit of the PID is added in the Appendix C. The output frequency of the VCO is linearly related to the control voltage, as illustrated in figure 5.8. Thus the locking points of the DFB laser can be shifted conveniently with the control voltage of the VCO. In addition, we point out that the capture range of the error signal is determined by $\pm 1/2t$, where t is the time delay caused by the cable. In our case with a 1-meter cable, the time delay is ~5 ns, thus the capture range is given by ~200 MHz. With a shorter cable the capture range can be increased but the slope of the error signal will be decreased, which results in a lower frequency resolution.

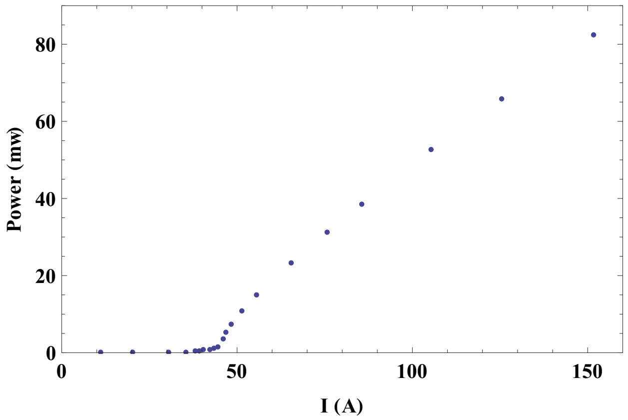

Figure 5.4: Threshold test of the DFB laser, which gives a threshold current of ∼46 mA.

5.3.3 Experimental Result

To judge whether the high field imaging work or not experimentally, one direct method is to drive the transition between $|2,2\rangle \rightarrow |3,3\rangle$ state at high magnetic field. In figure 5.9, we show a typical experimental result by measuring the peak OD with varying output frequency of the VCO hence the locked DFB laser frequency at 347 G. The data is fitted to a Lorentz function and the fitted result gives a width of 5.1 MHz.

5.4 Conclusion

In summary, the laser system for high field imaging is presented in this chapter. We start by the importance of the high field imaging system and the analysis of the energy shift of the D_2 line of both ^{87}Rb and Na. Then the design and set up of the DFB laser is described in detail. The DFB laser is locked to the trap laser for Rb laser cooling via the frequency offset locking scheme, with which its frequency can be tuned conveniently. At last the imaging system is verified with a simple experiment performed at 347 G.

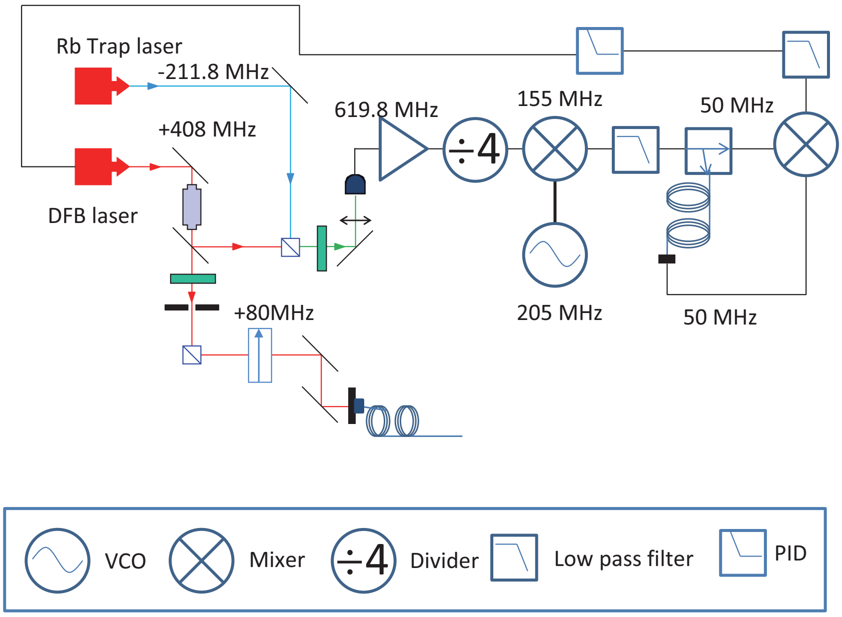

Figure 5.5: Optical layout of the offset locking scheme.

☐ End of Chapter.

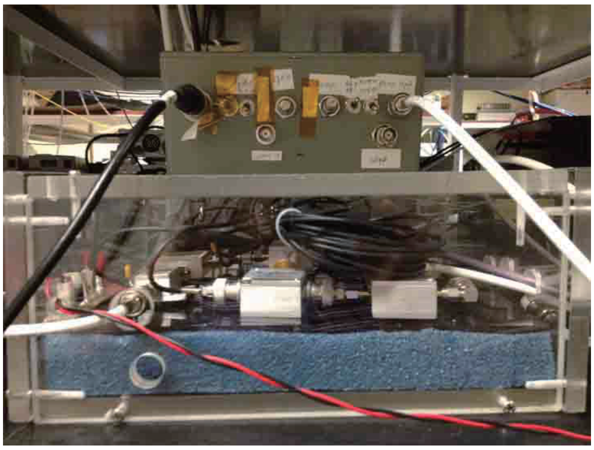

Figure 5.6: The real setup of the RF components of the offset locking scheme.

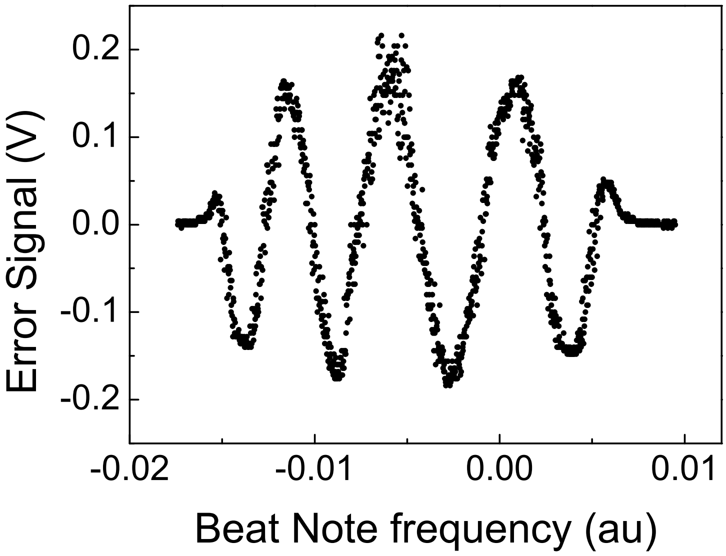

Figure 5.7: Error signal varying as a function of the beat note frequency. The zero crossings provides the locking position for the DFB laser.

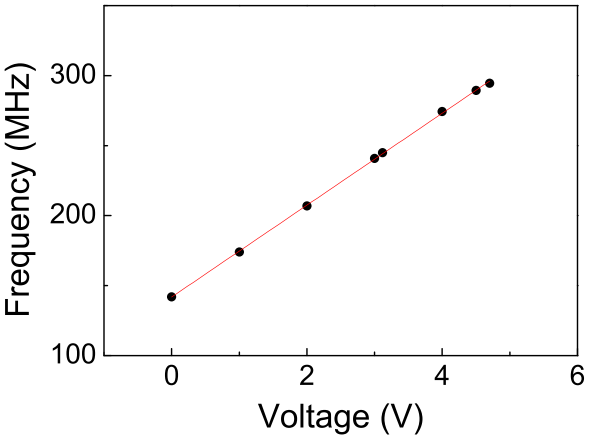

Figure 5.8: A test of the relationship between the control voltage and the output frequency of the VCO.

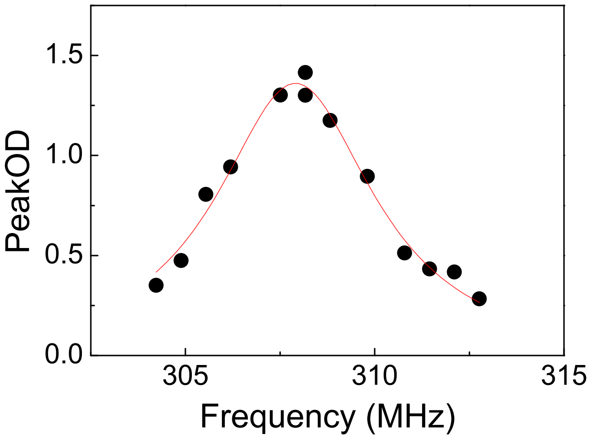

Figure 5.9: Test of the high field imaging by driving the transition between $|2,2\rangle \leftrightarrow |3,3\rangle$ state at 347 G with different output frequency of the VCO hence the locked DFB laser frequency. The dot is the experimental data and the red line is the Lorentz fitting.

Chapter 6

A “Magic Wavelength” Optical Trap for ^{87}Rb and Na

6.1 Overview and Motivation

From the above experimental results, the multi-wavelength optical trap seems already nice enough for the experiment except for the gravitational sag. It not only breaks the symmetry of the trap in the vertical direction, but also leads to the separation of the cloud center between Rb and Na. Thus the Feshbach molecule formation efficiency may be lowered due to the poor overlap. From Eq.(4.19), the separation results from the different trap frequencies between Rb and Na in the optical trap, and can be eliminated with a “magic wavelength” trap in which

$$\omega_{Na} : \omega_{Rb} = \sqrt{U_{Na}/m_{Na}} : \sqrt{U_{Rb}/m_{Rb}} = 1. \tag{6.1}$$

In this chapter the “magic wavelength” will be calculated based on both the classical model and the semiclassical treatment. Then we will have a comparison between the two models in the aspect of the trap depth and trap frequency as well as the calculated “magic wavelength”. After that the detailed description of the setup of our “magic wavelength” trap will be introduced with focus on the design of the tapered amplifier (TA). Finally an outlook for this trap is given.

6.2 Calculation of the “Magic Wavelength”

6.2.1 Classical Model

Follow Eq.(4.15) and equate the trap frequency of Rb with that of Na in the y direction, we obtain the result as shown in figure 6.1, whereas the trap frequency of both the Rb atoms and the Na atoms in the y direction varying as a function of the trap wavelength is illustrated. The intersection position gives the “magic wavelength” of $\lambda = 942.8$ nm, which indicates that the gravitational sag is zeroed at this wavelength. Above this position the ratio in Eq.(6.1) exceeds 1, which indicates a tighter trap for Na than that for Rb. While below this position it corresponds to a tighter trap for Rb instead.

6.2.2 Semiclassical Model

The classical model in fact can be regarded as a two level system, however the real atoms have a complex sublevels, thus to be more accurately, the contribution from all the excited states to the energy shift of the ground state of the alkali metal atoms (^{87}Rb and Na in our case) should be involved.

From the perturbation theory, the energy shift of the atoms in the light field can be treated in the second order of the electric field, i.e. proportional to the field intensity [97, 87]. As a result the interaction Hamiltonian H_{int}

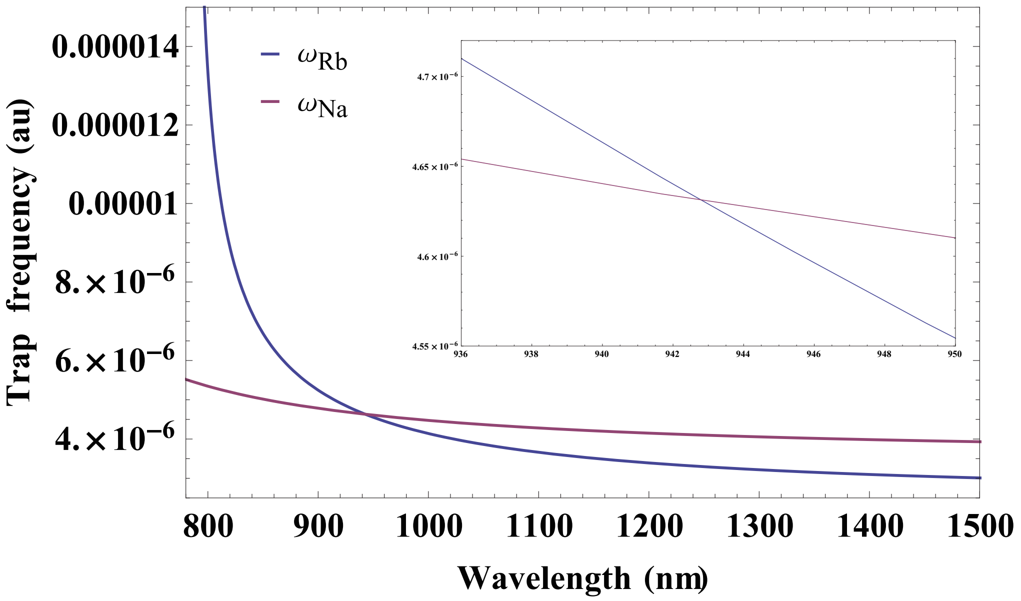

Figure 6.1: Trap frequency of ^{87}Rb and Na in the y direction as a function of the laser wavelength, the intersection gives a wavelength of $\lambda = 942.8$ nm, which indicates the “magic wavelength” where the Rb atoms and the Na atoms have the same trap frequency, thus zero the gravitational sag.

leads to the energy shift from the $i-$th upper level to the target ground level can be described as

$$\Delta E = \sum_{e_i} \frac{|\langle e_i|H_{int}|g\rangle|^2}{E_g - E_{e_i}}. \tag{6.2}$$

Here, the interaction Hamiltonian $H_{int} = -\hat{\mu}\vec{E}$, with $\hat{\mu}$ representing the electric dipole operator.

Eq.(6.2) can also be written in terms of the intensity of the laser field as [98]

$$\Delta E(x,y,z) = \frac{I(x,y,z)}{\epsilon_0 \hbar c} \sum_{e_i} |\langle e_i|\hat{\mu}|g\rangle|^2 \frac{\omega_{e_i g}}{\omega_{e_i g}^2 - \omega^2}, \tag{6.3}$$

where the dipole matrix element between the excited state $|e_i\rangle$ and the target ground state $|g\rangle$ is related to the spontaneous decay rate as

$$\Gamma = \frac{\omega^3}{3\pi\epsilon_0\hbar c^3}|\langle e_i|\hat{\mu}|g\rangle|^2. \tag{6.4}$$

From which one can see that with the known laser intensity and detuning the exact energy shift of the target ground state (for the excited state the energy shift just has a minus sign difference) can be obtained once the dipole moment is known. In the real experiment with the alkali metal atoms in a red detuned laser light field, the most relevant excited state related to the ground state is the D_1 and D_2 line, and the contribution from the higher excited states converge rapidly unless with a resonant wavelength [99]. Thus, a good approximation can be made by considering the doublet structure as the dominant while the higher excited states as the correction if necessary. With the effective dipole moment of 2.44 ea_0 (2.035 ea_0) (a_0 is the Bohr radius) for the D_2 line and 1.728 ea_0 (1.44 ea_0) for the D_1 line of ^{87}Rb (Na) [100], the trap potential and the trap frequency for both Rb and Na can be obtained. In figure 6.2, the calculated trap frequency for both the Rb atoms and the Na atoms in the y direction as a function of the trap wavelength is shown based on Eq.(6.3), which gives the “magic wavelength” of 945.828 nm.

A more accurate calculation involves the higher levels correction gives the “magic wavelength” of 946.466 nm with an accuracy of 0.5% [99], thus, one may see that both the two models are effective for finding the “magic wavelength” with the later one having a higher precision, i.e. much closer to the exact position. For the trap depth and the trap frequency, a comparison between the two models is also made with a single 1070 nm light with beam waist 50 μm and power 5 W. The results are shown in table 6.1, from which one can see that the classical model gives approximately the same trap

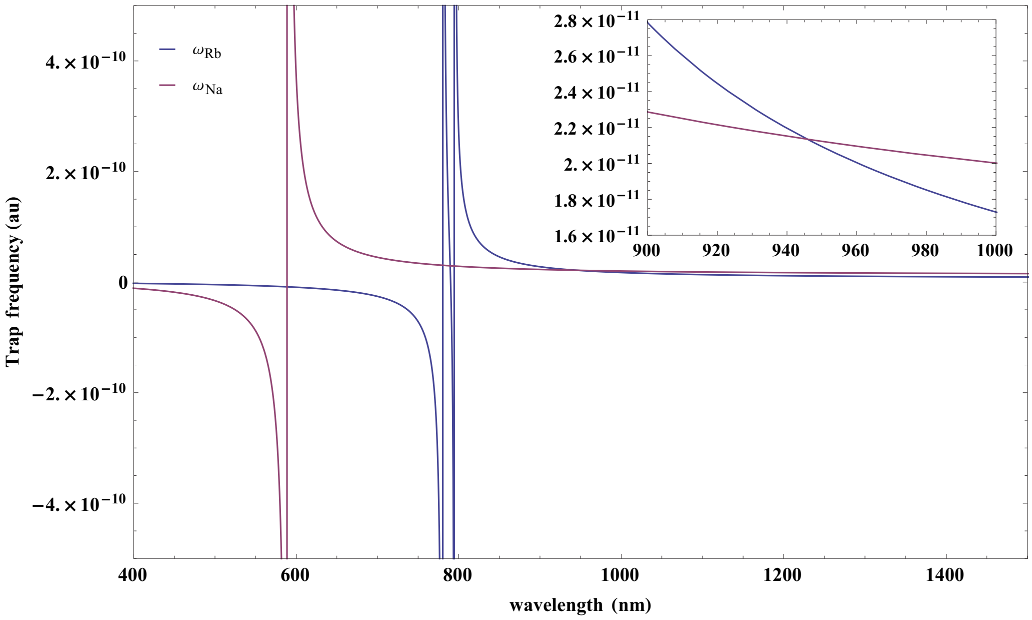

Figure 6.2: Trap frequency for both the Rb atoms and the Na atoms in the y direction varying with the trap wavelength, the intersect positions (except $\lambda \approx 589$ nm or 780 nm which corresponds to the resonance of Na and Rb) predicates the "magic wavelength" of 945.828 nm.

depth and trap frequency for the two species as the semiclassical model, thus accurate enough for helping control and understand the experiment process.

6.3 Tapered Amplifier Setup

The heart of the "magic wavelength" trap is the homemade tapered amplifier (TA) (m2k-laser GmbH) which is orientated in the external resonator configuration, as shown in figure 6.3. The TA chip is embed in the c-mount pocket with two facets, i.e. a rear facet with ridge-waveguide structure and a front facet with an anti-reflection coating. When fed with a current above ∼500 mA, there will be emitting light out from both the two facets of the chip with the one from the front facet, i.e. the output facet, stronger than

	Classical Model		Semiclassical Model	
	^{87}Rb	Na	^{87}Rb	Na
Trap Depth (μK)	189.6	66.0	191.3	66.0
Trap Frequency (Hz)	(857, 857, 4)	(984, 984, 5)	(861, 861, 4)	(984, 984, 5)
Magic Wavelength (nm)	942.816		945.828	

Table 6.1: Comparison between the classical model and the semiclassical model in terms of the trap depth and trap frequency for both the Rb atoms and the Na atoms with a single beam 1070 nm trap with beam waist 50 μm and power 5 W, as well as the precision in predicting the “magic wavelength” position.

that from the rear facet. The output light from the rear facet is used for optical feedback. A collimating lens (A397TM-B) is used to achieve a good coupling to the grating (GH13-12U), and a $\lambda/2$ waveplate is used to tune the polarization of the light to achieve the highest reflection efficiency from the grating, thus the highest coupling efficiency. In figure 6.4 the threshold current of the TA is test at wavelength ~946 nm, which gives a threshold of ~1.2 A. The slope of the TA is only ~670 mW/A, which is due to the fact that 946 nm is not at the center of the TA chip's gain profile. We have measured that above the threshold the output intensity at ~946 nm is only 70% of that at ~955 nm (central wavelength). With operating current of 2.8 A, the output power of the laser reaches 1 W.

Generally two pairs of cylindrical lens are needed to collimate the laser beam output from the front facet due to strong astigmatism as a result of the internal structure of the chip. In our setup, the laser beam is collimated with an aspheric lens (C330TME-B) and a cylindrical lens (LJ1402L2-B) in both directions and then telescoped by two times with a pair of singlet lenses (f = 100, -50 mm) to achieve a high diffraction efficiency of the AOM and a high fiber coupling efficiency, see figure 6.5.

Similar to the ECDL, to make the TA laser work in a single mode with low

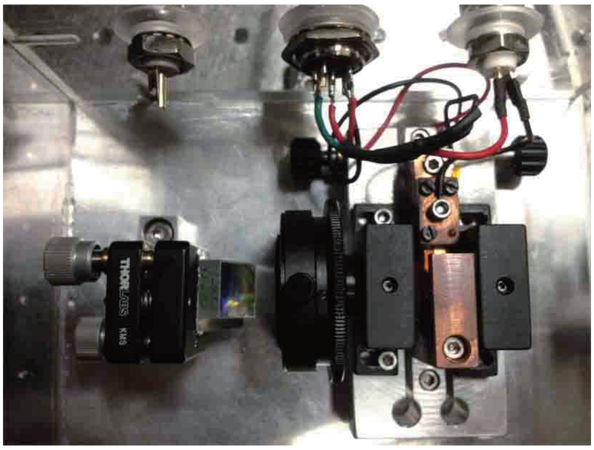

Figure 6.3: The real optical layout of the TA.

noise, a stable current driver and a temperature controller are also required. In this case the TA is driven by a 4-A current controller (Thorlabs LDC240C), and the temperature stabilization scheme is pretty similar to the one used in the ECDL.

6.4 Optical Layout

The optical layout of the “magic wavelength” trap is shown in figure 6.5. Compared with the setup of the multi-wavelength trap, see figure 4.4, the major difference is the application of an optical fiber used mainly as a mode filter. With optimized beam profile an overall efficiency of ∼50% of the setup has been achieved, involving the losses from the isolator, the AOM and fiber coupling. With 2.8 A operating current we can obtain a nice Gaussian beam with up to 500 mW power out from the fiber.

The “magic wavelength” trap is designed with a beam waist of $\sim 30\mu$m, so that a trap depth of ∼78 μK (∼21 μK) for Rb (Na) can be obtained with 500 mW power. This can provide a relative large trap volume for

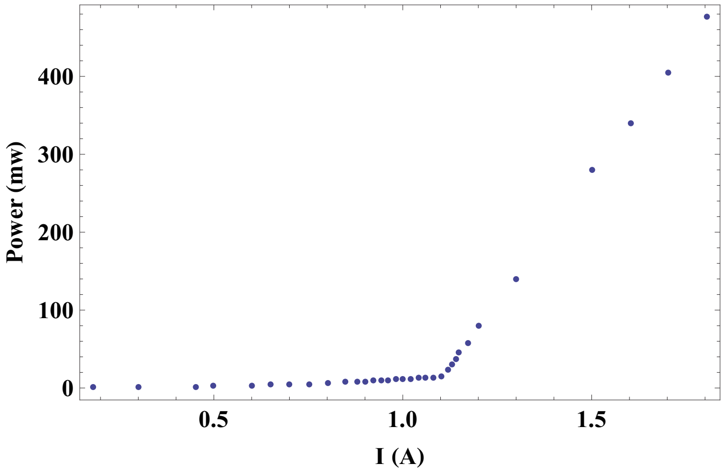

Figure 6.4: Threshold test of the TA laser at ∼946 nm, which gives a threshold of ∼1.2 A and a slope of ∼670 mW/A.

the loading process from the multi-wavelength trap after the evaporation process. A collimating lens (A397TM-B) together with a beam expander (f = 35, 100mm) is used to provide a suitable spot radius so that with a f = 300 mm lens a beam waist of 30 μm can be obtained. In figure 6.6, a typical measurement result of the beam waist of the “magic wavelength” trap is shown under this configuration, which gives a beam waist of 32 (33) μm in the horizontal (vertical) direction. We point out that with a diverging beam projected onto the final lens (f = 300 mm), a beam waist of 23 μm can be obtained. This means the trap size can be tuned conveniently by simply changing the relative distance between the f = 100mm lens and the f = 300 mm lens. In addition, by replacing the lens of f = 35 mm with a f = -30.0 mm one, one may even obtain a beam waist of 15 μm from the modeling results with the Zemax program.

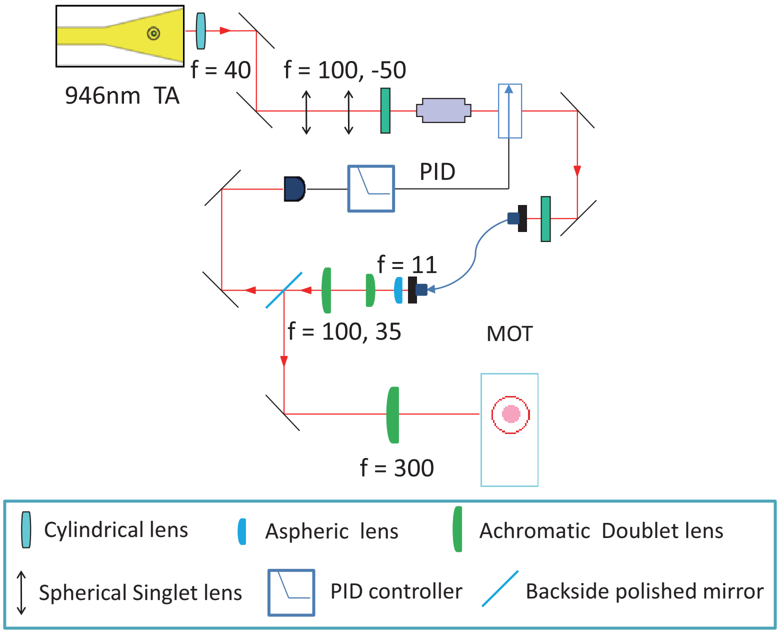

Figure 6.5: Optical layout of the “magic wavelength” trap. The f = 40 mm cylindrical lens together with the f = 3.1 mm aspheric (inside the laser box) and the telescope (singlet, f = 100, -50) is used to help increase the beam quality output from the laser to achieve a high diffraction efficiency of the AOM and a good coupling efficiency of the fiber. Another lens group is used to collimate and expand the output beam from the fiber to achieve a small beam waist near 30μm. The intensity stability scheme is the same as that in the multi-wavelength trap in chapter 4.

6.5 Conclusion and Outlook

Due to the limited time, the experimental verification of the “magic wavelength” trap is not finished, thus I just give a short summarize of the theoretical results and an outlook here.

In the “magic wavelength” trap, the trap frequency seen by the Na atoms and the Rb atoms will be the same, as shown in figure 6.2, thus the gravitational sag will be zeroed and a concentric cloud of the double BEC can be expected. In addition, an improvement of Feshbach molecule number is also

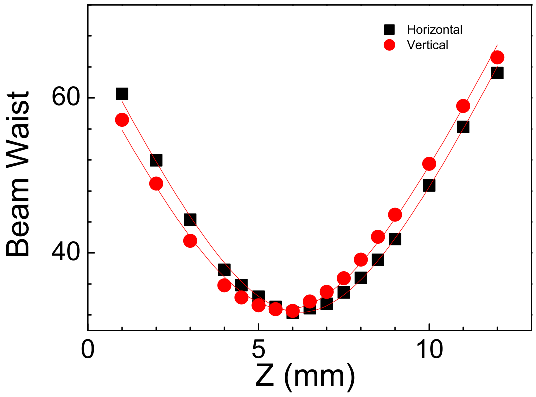

Figure 6.6: Typical beam profile of the “magic wavelength” trap. In this setup an optical fiber (Thorlabs P5-1064 pm -FC-2) is used as a mode filter to achieve a nice Gaussian profile. Then the laser beam is collimated by an aspheric Lenses (A397TM-B).

expected due to a better overlap of the atom cloud between Na and Rb.

□ End of Chapter.

Chapter 7

Conclusion and Outlook

7.1 Summary

In this thesis the apparatus of the ^{23}Na^{87}Rb mixtures experiment is described with focus on the multi-wavelength optical dipole trap. With the generally used crossed 1070 nm optical dipole trap, a quasi-pure double BEC with atom number of 5.0 $\times 10^4$ (2.5 $\times 10^4$) Na (Rb) can be achieved, while further optimization of the atom number is limited by the much shallower trap depth for Na than that for Rb, thus a single trap beam of the 660 nm trap is proposed. The basic idea behind this setup is to achieve a tuneable trap depth between Na and Rb atoms, or more accurately to keep the trap depth for Na equal or a little deeper than that for Rb, so that the Rb atoms can work as the coolant right after loaded into to the optical trap, hence much less lost of Na can be expected and much more number of Rb can be loaded into the trap.

With the improvement from the multi-wavelength trap and continually optimization of the system, we have observed the first Feshbach molecule signal at 347.75 G after removing the residual atoms with the gradient field.

To detect the molecules directly at high magnetic field, a new imaging system is designed based on a homemade DFB laser. This laser is locked to the trapping laser via the offset locking scheme and has a capture range of ~200 MHz. An experimental verification of the imaging system is performed by driving the cycling transition at 347 G. We point out that this laser can also be used to blast the residual atoms in combination with a RF pulse in the molecule formation stage.

On the other hand, due to the gravitational sag we have observed that the Rb BEC always locates below the Na BEC instead of a concentric double BEC pattern. To address this problem, the "magic wavelength" trap is proposed based on the semiclassical calculation. With this trap, the double BEC is expected to have a concentric structure.

7.2 Suggestion of Future Works

The 660 nm trap is not only useful for the production of Feshbach molecules in our system, the repulsive force to the Rb atoms makes it useful to study lots of physical topics, such as the soliton formation [101, 102, 103, 104], collective excitation [105], and Faraday wave [106, 107] in the dual species BEC, especially in combination with the "magic wavelength" trap. Though they all have been studied ever since the first observation of the BEC, there are still many quite interesting problems remained to be solved. Taking the study of solitons as an example, many interesting topics have been proposed, such as the properties of the solitons with thermal and fluctuations, the reflectivity or transitivity of a soliton interacting with a barrier potential [108], the collision properties of the dark-dark and dark-bright solitons in a double species BEC [109, 110, 111, 112], the properties of a soliton under a nonlinear environment [113, 114] or in a time dependent optical lattice [115, 116, 117, 118], et al.

In addition, the 660 nm laser has a stable single mode which makes it an ideal candidate for the setup of the optical lattice, which will further enrich our tool for the study of the above topics.

□ End of Chapter.

Appendix A

DC to DC Converter and Digital Isolator

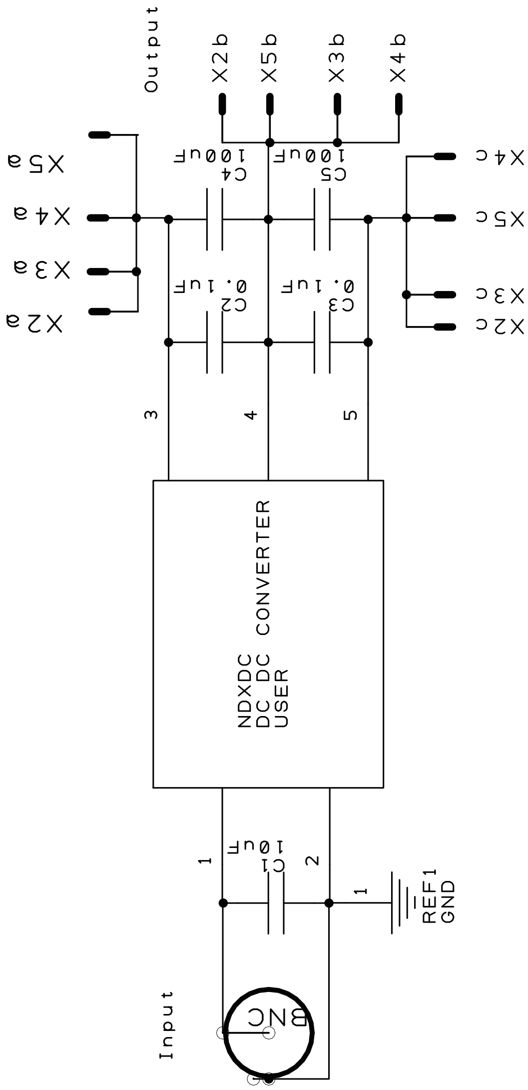

Figure A.1: DC to DC converter circuit.

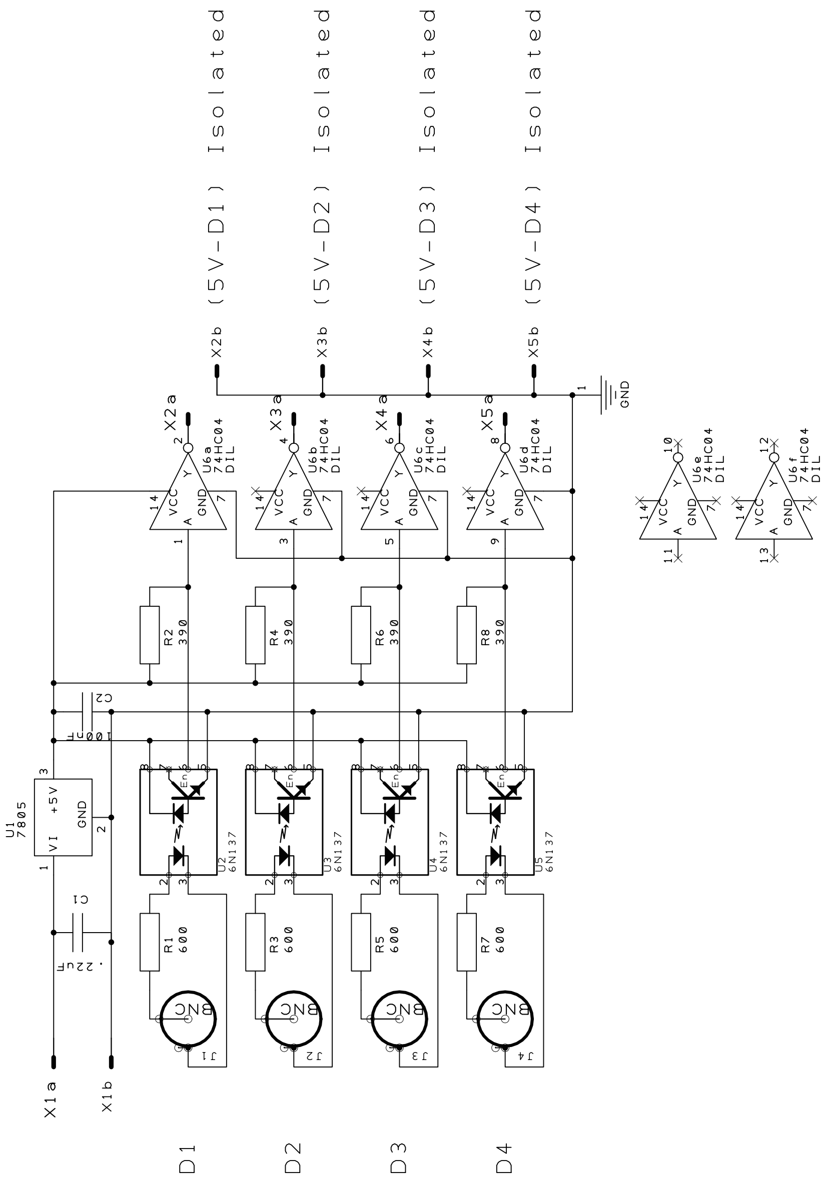

Figure A.2: Digital isolator circuit.

Appendix B

AOM Driver and Intensity Stabilization

B.1 AOM Driver

B.2 Intensity Stabilization PID

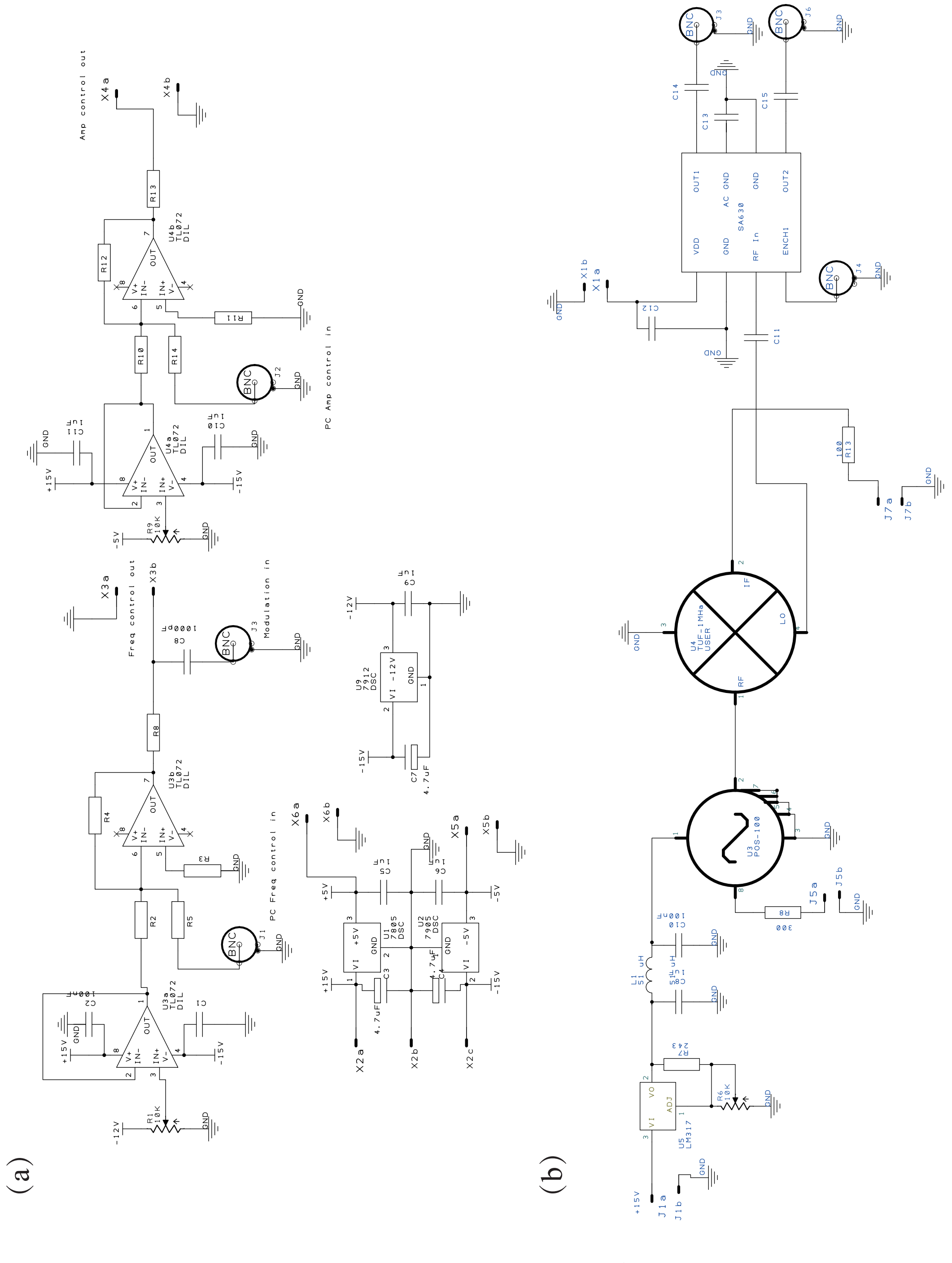

Figure B.1: Electronic circuit of the AOM driver.

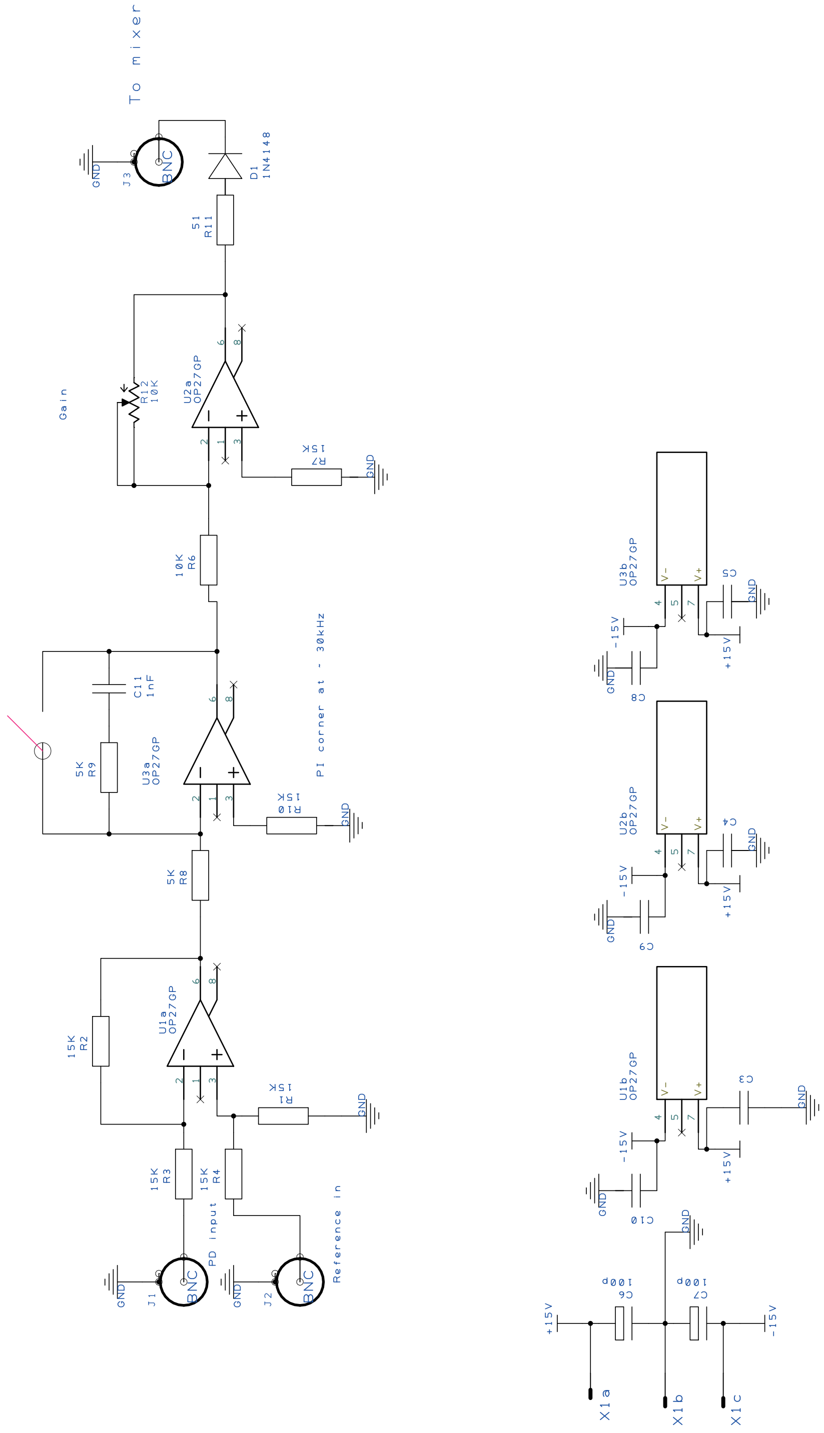

Figure B.2: The PID circuit for laser intensity stabilization.

Appendix C

DFB PID

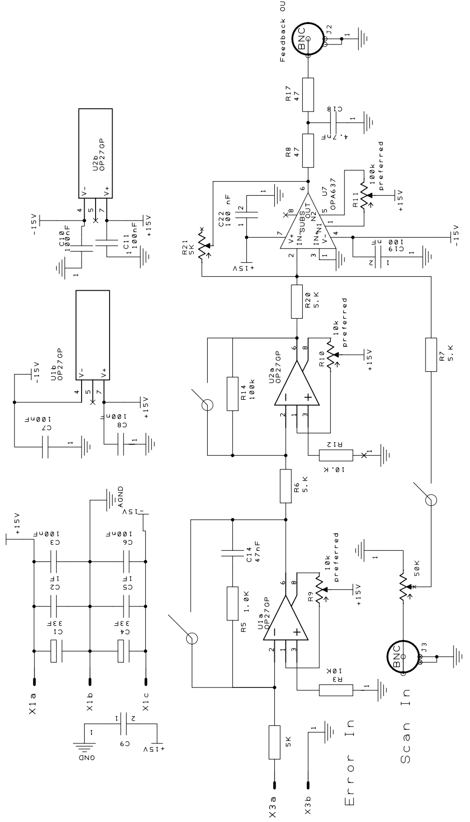

Figure C.1: Frequency Stabilization PID for DFB laser.

☐ End of Chapter.

Bibliography

[1] D. Xiong, X. Li, F. Wang, and D. Wang, arXiv:1305.7091 (2013).

[2] M.-S. Heo et al., Phys. Rev. A **86**, 021602 (2012).

[3] Bose, Zeitschrift für Physik **26**, 178 (1924).

[4] A. Einstein, Sitzungsber. Kgl. Preuss. Akad. Wiss. **261** (1924).

[5] M. H. Anderson, J. R. Ensher, M. R. Matthews, C. E. Wieman, and E. A. Cornell, Science **269**, 198 (1995).

[6] K. B. Davis et al., Phys. Rev. Lett. **75**, 3969 (1995).

[7] C. C. Bradley, C. A. Sackett, and R. G. Hulet, Phys. Rev. Lett. **78**, 985 (1997).

[8] E. A. Cornell and C. E. Wieman, Rev. Mod. Phys. **74**, 875 (2002).

[9] W. Ketterle, Rev. Mod. Phys. **74**, 1131 (2002).

[10] S. Inouye, J. Andrews, M. R.and Stenger, H.-J. Miesner, D. M. Stamper-Kurn, and W. Ketterle, Nature **392**, 151 (1998).

[11] Z. F. Xu, Y. Zhang, and L. You, Phys. Rev. A **79**, 023613 (2009).

[12] Y. Shi, Phys. Rev. A **82**, 023603 (2010).

[13] Z. F. Xu, D. J. Wang, and L. You, Phys. Rev. A **86**, 013632 (2012).

[14] N. V. Hung, P. Ziń, M. Trippenbach, and B. A. Malomed, Phys. Rev. E **82**, 046602 (2010).

[15] R. Blit and B. A. Malomed, Phys. Rev. A **86**, 043841 (2012).

[16] W. Wen and G. Huang, Phys. Rev. A **79**, 023605 (2009).

[17] J. Sabbatini, W. H. Zurek, and M. J. Davis, Phys. Rev. Lett. **107**, 230402 (2011).

[18] F. Zhan, J. Sabbatini, M. J. Davis, and I. P. McCulloch, arXiv:1403.4823 (2014).

[19] M. Greiner, O. Mandel, T. Esslinger, T. W. Hänsch, and I. Bloch, Nature **415**, 39 (2002).

[20] K. Góral, L. Santos, and M. Lewenstein, Phys. Rev. Lett. **88**, 170406 (2002).

[21] H. P. Büchler et al., Phys. Rev. Lett. **98**, 060404 (2007).

[22] A. Micheli, G. Pupillo, H. P. Büchler, and P. Zoller, Phys. Rev. A **76**, 043604 (2007).

[23] G. Pupillo et al., Phys. Rev. Lett. **100**, 050402 (2008).

[24] D. DeMille, Phys. Rev. Lett. **88**, 067901 (2002).

[25] A. Micheli, G. K. Brennen, and P. Zoller, Nat Phys **2**, 341 (2006).

[26] J. Ye et al., Precision measurement based on ultracold atoms and cold molecules, in *Frontiers in Optics*, page LTuK2, Optical Society of America, 2006.

[27] N. Vanhaecke and O. Dulieu, Molecular Physics **105**, 1723 (2007).

[28] C.-H. Wu, J. W. Park, P. Ahmadi, S. Will, and M. W. Zwierlein, Phys. Rev. Lett. **109**, 085301 (2012).

[29] T. D. Cumby, R. A. Shewmon, M.-G. Hu, J. D. Perreault, and D. S. Jin, Phys. Rev. A **87**, 012703 (2013).

[30] C. Weber et al., Phys. Rev. A **78**, 061601 (2008).

[31] T. Takekoshi et al., Phys. Rev. A **85**, 032506 (2012).

[32] M. P. Köppinger et al., Phys. Rev. A **89**, 033604 (2014).

[33] A.-C. Voigt et al., Phys. Rev. Lett. **102**, 020405 (2009).

[34] K.-K. Ni et al., Science **322**, 231 (2008).

[35] T. Takekoshi et al., arXiv:1405.6037 (2014).

[36] A. Marte et al., Phys. Rev. Lett. **89**, 283202 (2002).

[37] S. Knoop et al., Phys. Rev. A **83**, 042704 (2011).

[38] M. Aymar and O. Dulieu, The Journal of Chemical Physics **122**, (2005).

[39] P. S. Żuchowski and J. M. Hutson, Phys. Rev. A **81**, 060703 (2010).

[40] F. Wang, D. Xiong, X. Li, D. Wang, and E. Tiemann, Phys. Rev. A **87**, 050702 (2013).

[41] A. Corney, *Atomic and Laser Spectroscopy*, Oxford Classic Texts in the Physical Sciences, OUP Oxford, 2006.

[42] E. Aleksandrov, M. Chaĭka, and G. Khvostenko, *Interference of atomic states*, Springer series on atoms + plasmas, Springer-Verlag, 1993.

[43] S. Chu, Rev. Mod. Phys. **70**, 685 (1998).

[44] C. N. Cohen-Tannoudji, Rev. Mod. Phys. **70**, 707 (1998).

[45] W. D. Phillips, Rev. Mod. Phys. **70**, 721 (1998).

[46] H. Metcalf and P. van der Straten, *Laser Cooling and Trapping*, Graduate Texts in Contemporary Physics, Springer New York, 1999.

[47] C. Foot, *Atomic physics*, Oxford master series in physics, Oxford University Press, 2005.

[48] J. Dalibard and C. Cohen-Tannoudji, J. Opt. Soc. Am. B **6**, 2023 (1989).

[49] P. J. Ungar, D. S. Weiss, E. Riis, and S. Chu, J. Opt. Soc. Am. B **6**, 2058 (1989).

[50] E. L. Raab, M. Prentiss, A. Cable, S. Chu, and D. E. Pritchard, Phys. Rev. Lett. **59**, 2631 (1987).

[51] W. H. Wing, Progress in Quantum Electronics **8**, 181 (1984).

[52] A. L. Migdall, J. V. Prodan, W. D. Phillips, T. H. Bergeman, and H. J. Metcalf, Phys. Rev. Lett. **54**, 2596 (1985).

[53] W. Petrich, M. H. Anderson, J. R. Ensher, and E. A. Cornell, Phys. Rev. Lett. **74**, 3352 (1995).

[54] D. E. Pritchard, Phys. Rev. Lett. **51**, 1336 (1983).

[55] W. Ketterle, D. S. Durfee, and D. M. Stamper-Kurn, cond-mat/9904034 (1999).

[56] Y.-J. Lin, A. R. Perry, R. L. Compton, I. B. Spielman, and J. V. Porto, Phys. Rev. A **79**, 063631 (2009).

[57] D. Xiong, F. Wang, X. Li, T.-F. Lam, and D. Wang, arXiv:1303.0333 (2013).

[58] J. Lawall et al., Phys. Rev. Lett. **75**, 4194 (1995).

[59] H. J. Lee, C. S. Adams, M. Kasevich, and S. Chu, Phys. Rev. Lett. **76**, 2658 (1996).

[60] W. Ketterle and N. V. Druten, Evaporative cooling of trapped atoms, in *Evaporative Cooling of Trapped Atoms*, edited by B. Bederson and H. Walther, volume 37 of *Advances In Atomic, Molecular, and Optical Physics*, pages 181 – 236, Academic Press, 1996.

[61] C. G. Townsend et al., Phys. Rev. A **52**, 1423 (1995).

[62] H. F. Hess, Phys. Rev. B **34**, 3476 (1986).

[63] H. F. Hess et al., Phys. Rev. Lett. **59**, 672 (1987).

[64] N. Masuhara et al., Phys. Rev. Lett. **61**, 935 (1988).

[65] A. E. Leanhardt et al., Science **301**, 1513 (2003).

[66] C. S. Adams, H. J. Lee, N. Davidson, M. Kasevich, and S. Chu, Phys. Rev. Lett. **74**, 3577 (1995).

[67] M. D. Barrett, J. A. Sauer, and M. S. Chapman, Phys. Rev. Lett. **87**, 010404 (2001).

[68] T. Weber, J. Herbig, M. Mark, H.-C. Nägerl, and R. Grimm, Science **299**, 232 (2003).

[69] Y. Takasu et al., Phys. Rev. Lett. **91**, 040404 (2003).

[70] G. Cennini, G. Ritt, C. Geckeler, and M. Weitz, Applied Physics B **77**, 773 (2003).

[71] D. Rychtarik, B. Engeser, H.-C. Nägerl, and R. Grimm, Phys. Rev. Lett. **92**, 173003 (2004).

[72] C. Pethick and H. Smith, *Bose-Einstein Condensation in Dilute Gases*, Cambridge University Press, 2002.

[73] V. Bagnato, D. E. Pritchard, and D. Kleppner, Phys. Rev. A **35**, 4354 (1987).

[74] E. Gross, Il Nuovo Cimento Series 10 **20**, 454 (1961).

[75] L. P. Pitaevsk, Soviet Physics JETP-USSR **13** (1961).

[76] M. D. Barrett, J. A. Sauer, and M. S. Chapman, Phys. Rev. Lett. **87**, 010404 (2001).

[77] C. Klempt et al., Phys. Rev. A **73**, 013410 (2006).

[78] B. P. Anderson and M. A. Kasevich, Phys. Rev. A **63**, 023404 (2001).

[79] S. N. Atutov et al., Phys. Rev. A **67**, 053401 (2003).

[80] C. E. Wieman and L. Hollberg, Review of Scientific Instruments **62**, 1 (1991).

[81] L. Ricci et al., Optics Communications **117**, 541 (1995).

[82] O. Nilsson, S. Saito, and Y. Yamamoto, Electronics Letters **17**, 589 (1981).

[83] G. C. Bjorklund, Opt. Lett. **5**, 15 (1980).

[84] M. Snadden, R. Clarke, and E. Riis, Optics Communications **152**, 283 (1998).

[85] T.-L. Ho and V. B. Shenoy, Phys. Rev. Lett. **77**, 3276 (1996).

[86] H. Pu and N. P. Bigelow, Phys. Rev. Lett. **80**, 1130 (1998).

[87] R. Grimm, M. Weidemüller, and Y. B. Ovchinnikov, Advances in Atomic Molecular and Optical Physics **42**, 95 (2000).

[88] A. Kazantsev, Zh. Eksp. Teor. Fiz **66**, 1599 (1974).

[89] R. J. Cook, Phys. Rev. A **20**, 224 (1979).

[90] J. P. Gordon and A. Ashkin, Phys. Rev. A **21**, 1606 (1980).

[91] J. D. Jackson, Classical electrodynamics, 1998.

[92] `http://www.optoscience.com/maker/gooch/pdf/IntroductionAO.pdf`.

[93] D. McCarron, A guide to acousto-optic modulators, Technical report, Technical report, Durham University, 2007.

[94] G. Thalhammer et al., Phys. Rev. Lett. **96**, 050402 (2006).

[95] E. Arimondo, M. Inguscio, and P. Violino, Rev. Mod. Phys. **49**, 31 (1977).

[96] Schünemann, U. and Engler, H. and Grimm, R. and Weidemüller, M. and Zielonkowski, M., Review of Scientific Instruments **70**, 242 (1999).

[97] C. Cohen-Tannoudji, J. Dupont-Roc, and G. Grynberg, *Atom-photon interactions: basic processes and applications*, Wiley-Interscience publication, J. Wiley, 1992.

[98] A. Yamaguchi, *Metastable State of Ultracold and Quantum Degenerate Ytterbium Atoms : High-Resolution Spectroscopy and Cold Collisions*, PhD thesis, Kyoto University, 2008.

[99] M. S. Safronova, B. Arora, and C. W. Clark, Phys. Rev. A **73**, 022505 (2006).

[100] D. A. Steck, Alkali d line data, `http://steck.us/alkalidata/`, 2010.

[101] S. Burger et al., Phys. Rev. Lett. **83**, 5198 (1999).

[102] J. Denschlag et al., Science **287**, 97 (2000).

[103] Z. Dutton, M. Budde, C. Slowe, and L. V. Hau, Science **293**, 663 (2001).

[104] B. P. Anderson et al., Phys. Rev. Lett. **86**, 2926 (2001).

[105] H. Pu and N. P. Bigelow, Phys. Rev. Lett. **80**, 1134 (1998).

[106] K. Staliunas, S. Longhi, and G. J. de Valcárcel, Phys. Rev. Lett. **89**, 210406 (2002).

[107] P. Engels, C. Atherton, and M. A. Hoefer, Phys. Rev. Lett. **98**, 095301 (2007).

[108] P. Engels and C. Atherton, Phys. Rev. Lett. **99**, 160405 (2007).

[109] C. Becker et al., Nat Phys **4**, 496 (2008).

[110] P. Öhberg and L. Santos, Phys. Rev. Lett. **86**, 2918 (2001).

[111] H. E. Nistazakis, D. J. Frantzeskakis, P. G. Kevrekidis, B. A. Malomed, and R. Carretero-González, Phys. Rev. A **77**, 033612 (2008).

[112] M. A. Hoefer, J. J. Chang, C. Hamner, and P. Engels, Phys. Rev. A **84**, 041605 (2011).

[113] F. K. Abdullaev and M. Salerno, Journal of Physics B: Atomic, Molecular and Optical Physics **36**, 2851 (2003).

[114] G. Theocharis, P. Schmelcher, P. G. Kevrekidis, and D. J. Frantzeskakis, Phys. Rev. A **72**, 033614 (2005).

[115] R. G. Scott et al., Phys. Rev. Lett. **90**, 110404 (2003).

[116] G. Theocharis, D. J. Frantzeskakis, R. Carretero-González, P. G. Kevrekidis, and B. A. Malomed, Phys. Rev. E **71**, 017602 (2005).

[117] P. Kevrekidis, D. Frantzeskakis, and R. Carretero-González, *Emergent Nonlinear Phenomena in Bose-Einstein Condensates: Theory and Experiment*, Springer Series on Atomic, Optical, and Plasma Physics, Springer, 2007.

[118] D. J. Frantzeskakis, Journal of Physics A Mathematical General **43**, 213001 (2010).